Protein synthesis inhibition and loss of homeostatic functions in astrocytes from an Alzheimer's disease mouse model: a role for ER-mitochondria interaction.

Running Title: Disproteostasis & ER-mitochondria interaction in AD astrocytes

Laura Tapella[1]*, Giulia Dematteis[1]*, Marianna Moro[1], Beatrice Pistolato[1], Elisa Tonelli[1], Virginia Vita Vanella[4], Daniele Giustina[1], Aleida La Forgia[1], Elena Restelli[2$], Elettra Barberis[4], Tito Cali[5], Marisa Brini[6], Salvatore Villani[1], Erika Del Grosso[1], Mariagrazia Grilli[1], Marcello Manfredi[4], Marco Corazzari[3], Ambra A Grolla[1], Armando A Genazzani[1#], Dmitry Lim[1#]

Affiliations

[1] Department of Pharmaceutical Sciences, Università del Piemonte Orientale "Amedeo Avogadro", Via Bovio 6, 28100, Novara, Italy;

[2] Istituto di Ricerche Farmacologiche Mario Negri IRCCS, via Mario Negri 2, 20156, Milan, Italy;

[3] Department of Health Science (DSS), Center for Translational Research on Autoimmune and Allergic Disease (CAAD) & Interdisciplinary Research Center of Autoimmune Diseases (IRCAD), Università del Piemonte Orientale "Amedeo Avogadro";

[4] Department of Translational Medicine, Center for Translational Research on Autoimmune and Allergic Diseases (CAAD), Università del Piemonte Orientale "Amedeo Avogadro".

[5] Department of Biomedical Sciences, Neuroscience Center (PNC), Centro Studi per la Neurodegenerazione (CESNE), University of Padua, Padova, Italy.

[6] Department of Biology, University of Padua, Padova, Italy, Centro Studi per la Neurodegenerazione (CESNE)

[$] Current address: Human Technopole, Milan, Italy.

[*] These Authors contributed equally.

[#] Correspondence should be sent to; Armando A Genazzani armando.genazzani@uniupo.it and Dmitry Lim dmitry.lim@uniupo.it, Tel.: +39-0321 375822.

Keywords: astrocytes; Alzheimer's disease; proteostasis; ER stress UPR; eIF2α; ER mitochondrial interaction;

ABSTRACT

Deregulation of protein synthesis and ER stress/unfolded protein response (ER stress/UPR) have been reported in astrocytes. However, the relationships between protein synthesis deregulation and ER stress/UPR, as well as their role in the altered homeostatic support of Alzheimer's disease (AD) astrocytes remain poorly understood. Previously, we reported that in astrocytic cell lines from 3xTg-AD mice (3Tg-iAstro) protein synthesis was impaired and ER-mitochondria distance was reduced. Here we show that impaired protein synthesis in 3Tg-iAstro is associated with an increase of p-eIF2α and downregulation of GADD34. Although mRNA levels of ER stress/UPR markers were increased two-three-fold, we found neither activation of PERK nor downstream induction of ATF4 protein. Strikingly, the overexpression of a synthetic ER-mitochondrial linker (EML) resulted in a reduced protein synthesis and augmented p-eIF2α without any effect on ER stress/UPR marker genes. *In vivo*, in hippocampi of 3xTg-AD mice, reduced protein synthesis, increased p-eIF2α and downregulated GADD34 protein were found, while no increase of p-PERK or ATF4 proteins was observed, suggesting that in AD astrocytes, both *in vitro* and *in vivo*, phosphorylation of eIF2α and impairment of protein synthesis are PERK-independent. Next, we investigated the ability of 3xTg-AD astrocytes to support metabolism and function of other cells of the central nervous system. Astrocyte conditioned medium (ACM) from 3Tg-iAstro cells significantly reduced protein synthesis rate in primary hippocampal neurons. When added as a part of pericyte/endothelial cell (EC)/astrocyte 3D co-culture, 3Tg-iAstro, but not WT-iAstro, severely impaired formation and ramification of tubules, the effect, replicated by EML overexpression in WT-iAstro cells. Finally, a chemical chaperone 4-phenylbutyric acid (4-PBA) rescued protein synthesis, p-eIF2α levels in 3Tg-iAstro cells and tubulogenesis in pericyte/EC/3Tg-iAstro co-culture. Collectively, our results suggest that a PERK-independent, p-eIF2α-associated impairment of protein synthesis compromises astrocytic homeostatic functions, and this may be caused by the altered ER-mitochondria interaction.

INTRODUCTION

Early cellular dysfunction during AD pathogenesis includes deregulation of Ca^{2+} homeostasis, mitochondrial dysfunction and bioenergetic deficit, oxidative stress and altered cell-cell communication. Such alterations may be traced back to the deregulation of protein synthesis, associated with the activation of endoplasmic reticulum (ER) stress/unfolded protein response (UPR), proposed as targets for the development of AD therapy [1–3]. Activation of ER stress/UPR has been reported in patients with advanced AD stages [4–7]. In cellular and animal AD models, heterogeneous and somewhat contrasting data have been reported and activation of ER stress/UPR in AD models has been debated [8]. The central element which links ER stress/UPR to the accumulation of misfolded proteins is represented by PRKR-like endoplasmic reticulum kinase (PERK)-dependent phosphorylation of eukaryotic initiation factor 2α (eIF2α). In turn, this protein inhibits assembly of ribosomal 43S preinitiation complex and imposes a global translational block, with a profound impact on neural cell physiology [9,10]. However, non-canonical variants of ER stress/UPR and their role in AD pathogenesis have been discussed [11,12]. While most of the reports consider neuronal mechanisms of ER stress/UPR in AD, contribution of astrocytes has been generally overlooked.

Astrocytes are homeostatic and secretory cells, whose function is to warrant the stability of the extracellular space, the development and correct functional integration of the CNS components in an environment which has recently been called the "active milieu" [13]. Therefore, the activation of ER stress/UPR and deregulation of protein synthesis in astrocytes would be particularly important for their potential role in CNS pathologies in terms of cellular dysfunction and loss of supportive functions. For example, local translation of mRNA in astrocytic processes is suggested to be important for shaping the repertoire of astrocytic plasma membrane and secreted proteins warranting support to neurons [14,15]. A derangement of ribosomal protein synthesis machinery in AD astrocytes has already been documented [4]. While a canonical [PERK → p-eIF2α → protein synthesis block] pathway is postulated in astrocytes, only fragmentary data are available. Moreover the relationships between ER stress/UPR and protein synthesis in astrocytes during AD progression remain largely unexplored [16].

Recently, we proposed immortalized hippocampal astrocytes from 3xTg-AD mice (3Tg-iAstro cells) as a novel cellular model which shows features of AD-like pathology, i.e., transcriptional and translations alterations, deregulation of Ca^{2+} signaling, bioenergetic deficit, elevated ROS and augmented ER-mitochondria interaction [17–21]. The central finding, linking the astrocytic cell pathology with possible deficit of homeostatic support, was protein synthesis impairment and a modest increase of ER stress/UPR related genes [19,20]. Herein we further investigated, both *in vitro* and *in vivo,* if reduction of protein synthesis in 3xTg-AD astrocytes was due to ER stress/UPR. Our results suggest that a PERK-independent, p-eIF2α-associated impairment of protein synthesis alters secretome of AD astrocytes and compromises their supportive and defensive functions, possibly through altered ER-mitochondria interaction.

RESULTS

Protein synthesis impairment in AD astrocytes is associated with PERK-independent phosphorylation of eIF2α in 3Tg-iAstro cells.

To investigate if protein synthesis impairment in 3Tg-iAstro cells was due to activation of [PERK → eIF2α → activating transcription factor 4 (ATF4)] axis, we first of all confirmed that 3Tg-iAstro have a significant reduction of protein synthesis, compared to WT-iAstro cells, using both immunocytochemical (ICC) (Fig. 1a) and Western blot (WB) analysis (Fig. 1b) of puromycin incorporation in neo-synthetized peptides (SUrface SEnsing of Translation (SUnSET) method [22,23]) (Fig. 1). Next, we investigated expression levels of p-eIF2α, whose de-phosphorylation is essential for the assembly of pre-initiation complex and initiation of translation [10]. As shown in Fig. 2a, the levels of p-eIF2α were significantly higher in 3Tg-iAstro compared with WT-iAstro cells, and comparable to levels in WT-iAstro and 3Tg-iAstro treated with thapsigargin (THG), an established ER stress/UPR inducer. We also measured expression levels of growth arrest and DNA damage-inducible gene 34 GADD34, a protein which provides a scaffold for eIF2α de-phosphorylation by protein phosphatase 1 (PP1) [9]. Surprisingly, GADD34 protein levels were significantly lower in 3Tg-iAstro compared to WT-iAstro cells (Fig. 2a). Next, we asked if augmented levels of p-eIF2α correlated with activation of PERK in our cellular model. However, the levels of p-PERK were not different in WT-iAstro and 3Tg-iAstro cells (Fig. 2b). During ER stress/UPR, activated and auto-phosphorylated PERK phosphorylates eIF2α and induces p-eIF2α-dependent upregulation of transcription factor ATF4 [9]. However, in 3Tg-iAstro levels of ATF4 were not different from those in WT-iAstro cells (Fig. 2b). Altogether these data suggested that phosphorylation of eIF2α in 3Tg-iAstro cells was not due to activation of [PERK → eIF2α/GADD34 → ATF4] axis. These results are in apparent contrast with our previous report of a two-three-fold transcriptional upregulation of ER stress/UPR-induced genes Atf4, spliced variant of X-box-binding protein 1 (Xbp1s) and homocysteine inducible ER protein with ubiquitin like domain 1 (Herpud1) in 3Tg-iAstro cells compared to its WT counterpart [20] . Therefore, we compared the induction of ER stress/UPR markers in 3Tg-iAstro cells with those induced by THG, which produces maximal induction of ER stress/UPR markers. We confirmed that in 3Tg-iAstro cells mRNA of the three ER stress/UPR markers significantly increased, and the increase was in line with our previous publications [20] (Fig. 3, middle histograms). However, the maximal upregulation of all three transcripts was much higher in THG-treated (1 μM, 4 h) vs non-treated cells than that in 3Tg-iAstro vs WT-iAstro (by 4.8 fold for Atf4, by 50-70 fold for Xbp1s and 18-25 fold for Herpud1) (Fig. 3, right histograms). Of note, there was a tendency to a lower THG-induced upregulation of Xbp1s and Herpud1 (mRNA, Fig. 3b,c right histograms), and ATF4 (protein, Fig. 2b) in 3Tg-iAstro compared with WT-iAstro, although the differences were not significative in the current experimental setting. To strengthen the result we assessed mRNA levels of other genes involved in different arms of ER stress/UPR response as well as UPR-inducible chaperons including Atf6, Ddit3/CHOP, Bip/Grp78, calreticulin and Dnajb9/ERdj4. As shown in Supplemental Fig. 1, essentially the same result was obtained. We concluded that eIF2α phosphorylation and

126 the reduction of protein synthesis in 3Tg-iAstro cells were PERK-independent, however a low-grade chronic
127 ER stress cannot be ruled out.

128 ***Reduction of protein synthesis and increase of p-eIF2α in astrocytes expressing a 10 nm ER-mitochondrial***
129 ***linker.***

130 Previously, we reported that ER-mitochondrial interaction, measured by SPLICS (split-GFP-based Contact
131 site Sensor), a recently developed ER-mitochondria contact sites sensor [24–26], is increased in 3Tg-iAstro
132 compared with WT-iAstro cells, suggesting a correlation between ER-mitochondrial distance and reduction of
133 protein synthesis [20]. To test the hypothesis of the causal role of the shorter ER-mitochondrial distance on
134 protein synthesis reduction we transfected WT-iAstro cells with a synthetic linker which fixes the ER-
135 mitochondria distance at about 10-12 nm (named as 10nm-EML) (a kind gift from György Csordás and György
136 Hajnóczky, Thomas Jefferson University). The linker was composed of monomeric red fluorescent protein
137 (mRFP) and an amino acidic liner, flanked at the N-terminal side by an ER-targeting sequence, and at the C-
138 terminal side by an outer mitochondrial membrane-targeting sequence [27]. We found that the expression of
139 10nm-EML significantly reduced protein synthesis rate as tested in the SUnSET assay, either by WB (Fig. 4a)
140 or ICC (Fig. 4c). Strikingly, 10nm-EML expression also significantly augmented p-eIF2α levels (Fig. 4b). At
141 this point, we checked if the reduction of protein synthesis and increase of p-eIF2α were paralleled by an
142 induction of ER stress/UPR marker genes. However, expression of Atf4, Xbp1s and Herpud1 transcripts were
143 not different between Ctr (WT-iAstro transfected with mRFP) and 10nm-EML-expressing WT-iAstro cells.
144 Altogether these data, in line with alterations found in 3Tg-iAstro cells, suggest that increased interaction
145 between ER and mitochondria augments phosphorylation of eIF2α and reduces protein synthesis by an UPR-
146 independent mechanism.

147 ***PERK-independent increase of p-eIF2α and protein synthesis reduction in vivo in 3xTg-AD mouse***
148 ***astrocytes.***

149 Next, we assessed if similar alterations in protein synthesis, p-eIF2α and ER stress markers could be found
150 also *in vivo* in the hippocampus of 3xTg-AD and WT mice. To assess protein synthesis rate, 3xTg-AD mice
151 were injected with puromycin (225 mg/Kg body weight) intraperitoneally (i.p.) for 1.5 h. Then hippocampi
152 were harvested and puromycin incorporation was analysed by WB and immunohistochemical analysis (IHC).
153 As shown in Fig. 5a, WB analysis showed a significantly reduced puromicyn-positive signal in 3xTg-AD mice
154 compared with WT. The result was confirmed by anti-puromycin staining of brain cryosections (Fig. 5b).
155 Assessment of [PERK → eIF2α/GADD34 → ATF4] axis activation by WB revealed significant increase of p-
156 eIF2α, reduction of GADD34 protein, while total PERK and ATF4 were not changed. Under the same
157 experimental conditions, p-PERK was undetectable by WB analysis in both genotype samples (Fig. 6a). This
158 result, and the absence of total PERK mobility shift, which accompany THG-induced PERK phosphorylation
159 in astrocytes (Fig. 2b), suggest that PERK is not activated in hippocampi of 3xTg-AD mice. IHC analysis
160 confirmed upregulation of p-eIF2α specifically in CA1 neuropil astrocytes of 3xTg-AD mice (Fig. 6b), while

GADD34 staining was diffused and was significantly reduced in the CA1 neuropil (Fig. 6c). qPCR analysis on whole hippocampal lysates revealed no changes in Atf4, Xbp1s, and Herpud1 transcript levels (Fig. 6d). Altogether, these data suggest that in AD astrocytes, both *in vitro* and *in vivo*, p-eIF2α-associated reduction of protein synthesis was independent of PERK activation but may be associated with alterations in ER-mitochondria interaction.

3Tg-iAstro cells do not support neuronal protein synthesis and pericyte-endothelial cell (EC) tubulogenesis in vitro, the effect, replicated by 10nm-EML.

Growing body of evidence suggest that non-cell autonomous mechanisms of neuronal degeneration during AD pathogenesis could be mediated by astroglia dysfunction and reduced homeostatic support to neurons and other cells in the CNS. Therefore, we assessed the effect of 3Tg-iAstro cells on neurons and a three-cell pericyte/EC/astrocyte 3D co-culture. 3Tg-iAstro-Conditioned Medium (ACM) transfer, but not WT-iAstro-ACM, onto primary murine hippocampal cultured neurons resulted in a significant reduction of neuronal protein synthesis, an early sign of neuronal dysfunction [28–31] (Fig. 7a and b). Treatment of neurons with ACM from WT-iAstro cells overexpressing 10nm-EML had also reduced protein synthesis rate (Fig. 7c). When WT-iAstro or 3Tg-iAstro cells were added as a component of pericyte/EC/astrocyte 3D co-culture, WT-iAstro, but not 3Tg-iAstro, supported formation of vessel-like tubules by pericyte and EC (Fig. 7d). Strikingly, the effect of 3Tg-iAstro was reproduced by co-culture with 10nm-EML-overexpressing WT-iAstro cells (Fig. 7d). These results suggest that alterations of astrocyte-derived soluble factors and cell-cell contact may account for 3Tg-iAstro inability to support neuronal protein synthesis and pericyte/EC tubulogenesis and that ER-mitochondria interaction may have a role.

Analysis of secretome from 3Tg-iAstro cells suggests impairment of neurogenic, neuroprotective functions and inter-cellular interaction.

In search of astrocyte-derived soluble factors we performed shotgun mass spectrometry proteomics of ACM from WT-iAstro and 3Tg-iAstro cells, followed by bioinformatic analysis. As shown in Supplemental Table 1, 120 and 84 proteins were identified, respectively, in WT- and 3Tg-iAstro cells ACM. Of these, 55 were expressed by both types of astrocytes, while 65 and 29 were identified only in WT- or 3Tg-iAstro cells ACM, respectively. Two pipelines of analysis have been performed. Firstly, proteins were quantified and differentially expressed proteins (DEPs) in 3Tg-iAstro vs WT-iAstro cells were identified (Supplemental Table 2). Five DEPs were identified. Of those, one, fatty acid-binding protein 3 (Fabp3) was upregulated, while four proteins, secreted protein acidic and cysteine rich (SPARC), heat shock protein 90 (HSP90), heat shock protein 73 (HSP73) and α1-tubulin, were significantly down-regulated in 3Tg-iAstro compared with WT-iAstro cells (Fig. 8, left table). SPARC is a pro-neurogenic factor released by astrocytes which promotes neuronal differentiation [32]. Extracellular heat shock proteins are known to be neuroprotective [33]. Specifically, extracellular HSP90 protects neurons from oxidative stress [34]. Therefore, our proteomic results suggest that neurogenic and neuroprotective support in 3Tg-iAstro cells may be reduced compared with the WT

counterpart. In a separate analysis, uniquely identified proteins were considered and subjected to gene ontology (GO) analysis using DAVID online tool in search of overrepresented groups of proteins. This analysis revealed that WT-iAstro, but not 3Tg-iAstro secretome, was enriched in proteins involved in cell-cell contacts, focal adhesion contacts and constituents of extracellular matrix (ECM), suggesting that support of cell-cell communication and ECM formation may be impaired in 3Tg-iAstro cells (Fig. 8, right upper table). Next we investigated if manipulation with ER-mitochondrial distance or normalization of protein folding had an effect on the secreted proteins. 10nm-EML overexpression in WT-iAstro cells did not influence the identified proteins (Supplemental Table 3). However, treatment of 3Tg-iAstro cells with a chemical chaperone 4-PBA (4-phenil butyric acid) rescued the presence of proteins responsible for extracellular matrix formation (Fig.8 right bottom table and Supplemental Table 4).

A chemical chaperone rescues protein synthesis alterations, ER-mitochondrial interaction, and homeostatic defects of 3Tg-iAstro cells.

Our data suggest that impairment of protein synthesis may represent a key feature of astrocytic dysfunction in AD, which was accompanied by the increased interaction between ER and mitochondria [20,21]. Therefore we investigated if the correction of protein folding efficiency may be beneficial to mitigate the protein synthesis and ER-mitochondria interaction defects in 3Tg-iAstro cells using 4-PBA, an FDA approved small molecule that has shown a protective effect on the AD related neuropathology in several animal models [35,36]. Moreover, it has been proven that 4-PBA, due to its action as a chemical chaperone, can promote correct protein trafficking, folding and prevent protein aggregation [35]. Incubation of cell culture with 4-PBA (3 μM, 48 h), fully rescued both protein synthesis rate (Fig. 9a) and p-eIF2α levels (Fig. 9b) in 3Tg-iAstro cells. Moreover, ER-mitochondria interaction at 8-10 nm, measured with SPLICS, was significantly lower in 4-PBA-treated 3Tg-iAstro cells [20,24]. Strikingly, when 4-PBA-treated 3Tg-iAstro cells were plated together with pericyte/EC, effects on tubulogenesis were also reinstated (Fig. 9c). Importantly, 4-PBA treatment had no effect on pericyte/EC or pericyte/EC/WT-iAstro co-cultures. These data suggest that protein synthesis alterations compromise homeostatic functions in AD astrocytes and the improvement of astrocytic protein synthesis may rescue these alterations.

DISCUSSION

In the present report, we further investigated AD-related cellular alterations in a recently generated astrocytic AD model, WT- and 3Tg-iAstro cells [19,20]. Our results suggest that in hippocampal AD astrocytes, *in vitro* and *in vivo*, the reduction of protein synthesis is driven by phosphorylation of eIF2α independently of PERK activation. Our results also suggest that p-eIF2α increase and reduction of protein synthesis may be associated with the altered ER-mitochondria interaction. We also show that 3Tg-iAstro cells exert a reduced support to primary neurons, impair pericyte/EC mediated tubulogenesis and have an altered repertoire of secreted proteins. Last, we show that improvement of protein folding in 3Tg-iAstro cells by a chemical chaperone

231 rescued p-eIF2α levels, protein synthesis, ER-mitochondrial interaction and tubulogenesis in a three-cell
232 pericyte/EC/astrocyte co-culture.

233 ***PERK-independent eIF2α phosphorylation and protein synthesis inhibition in 3Tg-iAstro cells.***

234 The novel finding of this work is represented by the PERK-independent phosphorylation of eIF2α in an
235 astrocytic cellular model of AD. Phosphorylation of eIF2α is a central switch for translation inhibition during
236 the integrated stress response (ISR) and ER stress/UPR [9,10]. At the present stage of knowledge four kinases are
237 implicated in eIF2α phosphorylation during ISR, depending on the stress stimulus. PERK phosphorylates
238 eIF2α in response to the ER accumulation of misfolded/unfolded proteins, alterations of ER Ca^{2+} levels or
239 impairment of protein secretion machinery, which are the principal causes of ER stress [9,37]. Protein kinase
240 RNA-activated (PKR) has been shown to phosphorylate eIF2α in response to viral infection. General control
241 non-derepressible 2 (GCN2) kinase is activated in response to amino acid starvation; while heme-regulated
242 inhibitor (HRI) was initially shown to be activated by heme deprivation and to be an important component of
243 ISR induced by oxidative or osmotic stress, heat shock, and proteasome inhibition. All these kinases have been
244 implicated in AD pathogenesis [7,38–40]. Therefore, further experiments are necessary to investigate their role in
245 phosphorylation of eIF2α *in vitro* in 3Tg-iAstro cells. GADD34 is required for PP1 phosphatase to interact
246 with and dephosphorylate PERK and is a stress-inducible protein downstream of ATF4 [9]. Downregulation of
247 GADD34 both in 3Tg-iAstro cells and in hippocampi of 3xTg-AD mice corroborates the conclusion on PERK-
248 independent eIF2α phosphorylation and suggests that it may account for the increased p-eIF2α.

249 ***Increased ER-mitochondria interaction as a cause of impaired protein synthesis in iAstro.***

250 A mounting body of evidence suggests that the ER-mitochondria interaction is increased in AD, and this may
251 be linked to Ca^{2+} signaling deregulation, an important part of AD-related astrocytic dysfunction [21,41–45]. Our
252 results suggest that the impairment of protein synthesis, which is an important feature of early AD pathogenesis
253 in both neurons and astrocytes [46–48], may also be caused by the augmented interaction between ER and
254 mitochondria. The overexpression of a synthetic linker, which fixes the distance between ER and mitochondria
255 at about 10-12 nm, faithfully reproduced the phosphorylation of eIF2α, the impairment of protein synthesis in
256 absence of overt activation of ER stress/UPR. These results corroborate our previous finding on the increase
257 of mitochondria-ER contact sites (MERCS) at a short distance of 8-10 nm, as measured by SPLICS sensor
258 [20,24]. The mechanisms whereby shortening of the ER-mitochondria distance may result in phosphorylation of
259 eIF2α and impairment of protein synthesis remain currently unknown. It can be speculated that the disruption
260 of a physiological distance between two organelles alters ribosomal localization and/or integrity, resulting in
261 phosphorylation of eIF2α and impairment of assembly of the pre-initiation complex. Another mechanism may
262 involve a reduction of ATP synthesis downstream of the impaired ER-mitochondria Ca^{2+} transfer [20,21,49], since
263 protein metabolism is one of the most energy-consuming cellular activity (accounting for about 20% of overall
264 cell energy consumption) [50]. Further experiments are necessary to investigate how ER-mitochondria interaction
265 may impact on the protein synthesis machinery.

266 ***Loss of homeostatic support by 3Tg-iAstro.***

267 According to the current view on the role of astrocytic dysfunction in AD progression in terms of loss of
268 homeostatic support, a "good" astrocytic AD cell model should provide a "bad" support to other CNS cells.
269 This has been illustrated by us and other groups, e.g., showing that ACM from AD model mice produces
270 dysfunction and degeneration of cultured primary neurons [51–53]. In this frame, herein we show that, unlike WT-
271 iAstro ACM, ACM collected from 3Tg-iAstro cells impairs protein metabolism in cultured neurons. Moreover,
272 when plated together with pericytes and ECs in a 3D three-cell co-culture, unlike WT-iAstro, 3Tg-iAstro cells
273 do not allow formation of tubular structures, characteristic of "angiogenic" pericyte-EC co-cultures. Astrocytes
274 are known to secret factors supporting neurons in development and differentiation like thrombospondin 1,
275 SPARC, Sparcl1, and lipocalin-2 [32,54,55]. Astrocytes also secrete an array of proteins, including heat shock
276 proteins, acting as protective factors against different stress factors, including oxidative stress [33,56–58]. They also
277 express components of the ECM and adhesion molecules which support cell-cell communication and cellular
278 dynamics [59–61]. Strikingly, neurogenic SPARC and protective HSP90 and HSP73 were significantly reduced
279 in 3Tg-iAstro ACM compared with WT-iAstro ACM. In addition, proteins of cell adhesion and ECM were
280 overrepresented in WT- but not in 3Tg-iAstro ACM. Therefore, the proteomic analysis of 3Tg-iAstro
281 secretome strengthens the hypothesis of a reduced neurogenic and protective support and provides candidate
282 molecules and signals to be further studied and tested for the development of AD therapy.

283 ***Rescue of p-eIF2α, protein synthesis, ER-mitochondrial interaction and homeostatic support by 4-PBA.***

284 Our results suggest that a low-grade chronic ER stress, with a somewhat lower UPR response, albeit without
285 PERK activation, might exist in 3xTg-AD astrocytes. Although this is corroborated by rescue of protein
286 synthesis defect and p-eIF2α levels by a small chemical chaperone 4-PBA, these data are in an apparent
287 contradiction, because activation of PERK is regarded as an obligatory step in a protein misfolding-associated
288 UPR induction [9]. Of note, in this regard, that a low-grade chronic ER stress is characteristic for melanoma
289 cancer cells, and eIF2α phosphorylation may occur without ER stress [62,63]. Furthermore, although 4-PBA is
290 thought to act through prevention of protein aggregation in the ER, the full spectrum of its actions is not
291 completely understood [64]. Growing body of evidence suggest that the effect of 4-PBA can also be explained
292 from a Ca^{2+} handling point of view. 4-PBA has been shown to rescue THG- and tunicamycin-induced ER Ca^{2+}
293 depletion [65], to normalize ER-mitochondrial Ca^{2+} fluxes in the intervertebral discs nucleus pulposus cells
294 subjected to a compression-induced ER-stress [66], to abolish THG-induced cytosolic Ca^{2+} signals in pancreatic
295 acini [67] and to normalize cytosolic Ca^{2+} levels in 3-Chloro-1,2-propanediol (3-MCPD)-treated HEK293 cells
296 [68]. Moreover, 4-PBA has been shown to increase expression of SIGMA1R, a component and modulator of
297 MERCS [21,69]. These findings suggest that a direct or indirect action of 4-PBA on Ca^{2+} homeostasis and/or ER-
298 mitochondrial interaction could also be hypothesized. Indeed, here we show that the increased ER-
299 mitochondrial interaction in 3Tg-iAstro cells was fully rescued by 4-PBA. 4-PBA is an FDA approved drug
300 and it has been shown to ameliorate cognitive performance and AD-related neuropathology in AD mouse

301 models, holding a promise in AD therapy [35,36]. Therefore, a more detailed investigation of the 4-PBA
302 modulation of Ca^{2+} homeostasis and ER-mitochondria interaction is warranted.

303 **CONCLUSIONS**

304 ER stress/UPR has gained much attention as a possible target for drug development in AD [2,70–74]. However,
305 somewhat paradoxical results and discrepancies between models and human data on the activation of
306 components of the pathway, made the activation of ER stress/UPR in AD in its canonical form disputable [2,8,12].
307 To add to the complexity of the phenomenon, ER stress/UPR in neurodegenerative diseases has mostly been
308 studied or interpreted through the lens of a neuronal dysfunction, while for other CNS cells, in particular
309 astrocytes, only fragmentary data are available, which makes it difficult to draw a "whole picture" [16]. Although
310 deregulation of protein synthesis is well documented as an early feature of AD astrocytes, the relationships
311 between p-eIF2α, disproteostasis, and their link to ER-mitochondria communication, remain poorly
312 understood. Our data suggest that the deregulation of protein synthesis in a model of AD astrocytes may
313 involve p-eIF2α-associated inhibition of protein synthesis without an overt activation of PERK-mediated UPR.
314 Herein we propose that this defective pathway may be caused by a complex array of events, including altered
315 ER-mitochondria interaction.

316

317 **MATERIALS AND METHODS**

318 ***3xTg-AD mice***

319 3xTg-AD mice and non-transgenic controls (WT) were housed in the animal facility of the Università del
320 Piemonte Orientale, with unlimited access to water and food. Animals were managed in accordance with
321 European directive 2010/63/UE and with Italian law D.l. 26/2014. The procedures were approved by the local
322 animal-health and ethical committee (Università del Piemonte Orientale) and were authorized by the national
323 authority (Istituto Superiore di Sanità; authorization numbers N. 22/2013). All efforts were made to reduce the
324 number of animals by following the 3R's rule.

325 ***Immortalized hippocampal astrocytes from WT and 3xTg-AD mice.*** Generation of immortalized astrocytes
326 from hippocampi of WT and 3xTg-AD mice (WT- and 3Tg-iAstro cells) was described elsewhere [19]. iAstro
327 lines were maintained in complete culture media containing Dulbecco's modified Eagle's medium (DMEM;
328 Sigma-Aldrich, Cat. D5671) supplemented with 10% fetal bovine serum (Gibco, Cat. 10270) (FBS), 2 mM L-
329 glutamine (Sigma-Aldrich), and 1% penicillin/streptomycin solution (Sigma-Aldrich). Cells were passaged
330 once a week and used for experiments between passages 12 and 20 from establishment.

331 ***Pericytes and endothelial cells.*** Human immortalized pericytes (CL 05008-CLTH) and endothelial cells
332 EA.hy926 (CRL-2922™) were cultured in Dulbecco's modified Eagle's medium (DMEM; Sigma-Aldrich,
333 Cat. No. D5671) supplemented with 10% fetal bovine serum (Gibco, Cat. No. 10270) (FBS), 2 mM L-

334 glutamine (Sigma-Aldrich), and 1% penicillin/streptomycin solution (Sigma-Aldrich) at 37°C in 5% CO2.
335 Cells were used between passages 5 to 15 and passed twice a week.

336 ***Hippocampal neuronal cultures***. Mouse neuronal primary cultures were prepared as described previously
337 [17,52,75] with slight modifications. After enzymatic and mechanical dissociation, final cellular pellet was
338 resuspended in neurobasal A medium (Invitrogen, Cat. 10888022) supplemented with 2% B27 supplement
339 (Invitrogen, Cat. 17504044), 2 mg/mL glutamine, 10 U/mL penicillin, and 100 mg/mL streptomycin, and
340 plated as described above. Half of medium volume was changed every third day and the cells were lysed at
341 days in vitro (DIV) 15.

342 ***Cell transfection.*** $3x10^4$ cells/well (WT- or 3Tg-iAstro) were resuspended in 250 µl of complete DMEM and
343 250 µl of transfection mix, and plated onto 13 mm glass coverslips in 24 well plates. For the transfection mix
344 Lipofectamine 2000 (Thermo Fisher Scientific, Cat. 11668-019) and plasmid, in ratio 1:1, were mixed in
345 Optimem (Gibco, Cat. 11058-021); after 3 h, transfection medium was replaced with complete medium. After
346 48 h, cells were washed with PBS and fixed in 4% formaldehyde (Sigma, Milan, Italy). A 10 nm ER-
347 mitochondrial linker, which fixes the ER-mitochondrial distance at 10-12 nm, a modification of a 5 nm ER-
348 mitochondrial linker [27], was a kind gift from Drs György Csordás and György Hajnóczky (Thomas Jefferson
349 University). Generation of split-GFP contact sites sensor (SPLICS) was described elsewhere [24,25]

350 ***Astrocytes Conditioned Medium (ACM) preparation.*** For the preparation of ACM, $5x10^4$ WT-iAstro and 3Tg-
351 iAstro cells were plated in a 6 well-plate. After 24 h the media was changed with DMEM completed with FBS,
352 2 mg/mL glutamine, 10 U/mL penicillin, and 100 mg/mL streptomycin, or neurobasal A medium (Invitrogen,
353 Cat. 10888022) supplemented with 2% B27 supplement (Invitrogen, Cat. 17504044), 2 mg/mL glutamine, 10
354 U/mL penicillin, and 100 mg/mL streptomycin. 48h later, the media were collected and centrifuged at 12,000
355 g, for 10 min at 4°C. ACM was stored at -80°C [52,54].

356 ***Cell treatment with 4-phenylbutiric acid (4-PBA).*** WT-iAstro and 3Tg-iAstro cells were plated, and after 24h
357 were treated with 3µM 4-PBA (Sant Cruz Biotechnology, Cat. sc-232961) [62,76]. 48h later cells were lysated
358 and then used for WB analysis.

359 ***Cell treatment with thapsigargin.*** $5x10^4$ WT-iAstro or 3Tg-iAstro cells were plated in a 6MW dish. 48h later
360 they were acutely treated with thapsigargin (Tocris, Cat. 1138) (THG)**.** For WB analysis cells were treated
361 with THG 1 µM, for 1 h; for RNA extraction cells were treated with THG 1 µM for 4 h [62].

362 ***Pericytes/EC/astrocyte co-culture.*** For tubulogenesis assessment, a Matrigel synthetic extracellular matrix
363 (Corning, Cat. 356234) was used. 96 well plates were coated with 50 µl of Matrigel, gelatinized at 37°C for
364 30 min. Pericytes (CL 05008-CLTH, Celther Polska, Lodz, Poland), EA.hy926 (CRL-2922, ATCC) and WT-
365 iAstro or 3Tg-iAstro cells, in ratio 1:1:1 were resuspended in 100 µl of complete DMEM and plate on the

366 matrix at the density of $1x10^4$ cells/well, and incubated for 8 h. Phase contrast images were acquired with a
367 Zeiss 710 confocal laser scanning microscope.

368 ***SUnSET for assessment of protein synthesis.*** Global protein synthesis rate was assessed using the Surface
369 Sensing of Translation (SUnSET) method, as previously published [77]. Briefly, cells were incubated with 4 µM
370 puromycin dihydrochloride (Sigma, Cat. P8833) supplemented in normal medium at 37 °C with 5% CO_2 for
371 3 h. Subsequently, cell lysates were fixed for immune fluorescence analysis or western blot analysis [20,22]. WT
372 and 3xTgAD mice were i.p. injectd with puromycin dihydrochloride 225 mg/Kg body weight, n = 2 WT or
373 3xTgAD [78]. After 1.5 h, mice were anesthetized with i.p. injection of Zoletil (80 mg/kg) and Xylazine (45
374 mg/kg) and intracardially perfused with cold PBS. Brains were dissected and half of brains were used for WB
375 analysis and the other halves of brain were post-fixed in 4% paraformaldehyde. Coronal 40 µm thick
376 cryosections were used for immunochemical staining.

377 ***Immunofluorescence (IF).*** WT-iAstro and 3Tg-iAstro cells, grown onto 13 mm glass coverslips, were treated
378 as previously explained. Immunofluorescence was done as follows. Cells were fixed in 4% paraformaldehyde
379 and 4% sucrose, permeabilized (7 min in 0.1% Triton X-100 in phosphate-buffered saline (PBS)), blocked in
380 0,1% gelatine, and immunoprobed with an appropriate primary antibody over night at 4°C. After 3 times
381 washing in PBS, an Alexa-conjugated secondary antibody (1:200) was applied for 1 h at room temperature
382 (RT). The following primary antibody was used: anti-Puromycin (Millipore, Cat. MABE343). Secondary
383 antibody was Alexa Fluor 488 anti-mouse IgG. Nuclei were counter-stained with 4′,6-diamidino-2-
384 phenylindole (DAPI).

385 ***Quantitative fluorescence image analysis***. Images were acquired using a FV-1000 Olympus laser confocal
386 scanning system, Zeiss 710 confocal laser scanning microscope, Leica SP8 LIGHTNING Confocal
387 Microscope imaging systems and Leica Thunder imager 3D live cell. Images were acquired under non
388 saturating conditions and analysed with Fiji ImageJ 1.52p software. To determine the amount of the puromycin
389 labelled peptides on i-Astro, the puromycin mean fluorescence was measured for each selected cells excluding
390 nucleus and expressed as fold change relative to control. To determine the amount of the puromycin labelled
391 peptides on neuronal cultures and transfected i-Astro, the puromycin fluorescence was measured for the entire
392 cell area excluding nucleus as a corrected total cell fluorescence (CTCF) = Integrated Density — (Area of
393 selected cell X Mean background fluorescence). Data are expressed as fold change relative to control. For
394 Puromycin IHC quantification, the puromycin mean fluorescence was measured by setting threshold analysis.
395 Data are expressed as fold change relative to Ctr. For tubulogenesis assessment, the number of nodes taken
396 with Leica Metafluor software was divided for the area covered by cells, analysed with Fiji ImageJ 1.52p
397 software. The area covered by cells was expressed as the difference between the entire area and the closed area
398 delimited by the tubules. Quantification of SPLICS fluorescence was performed as described elsewhere [20].

Western Blot. Astroglial cultures or neuronal cultures were lysed with 100µL of lysis buffer (50mM Tris-HCl (pH 7.4), sodium dodecyl sulphate (SDS) 0.5%, 5mM EDTA, 10 µL of protease inhibitors cocktail (PIC, Millipore, Cat. 539133) and phosphatase inhibitor cocktail (Thermo Fisher Scientific, Cat. 78428) and collected in a 1.5 ml tube. Lysates were boiled at 96°C for 5 minutes and then quantified with QuantiPro BCA Assay Kit (Sigma, Cat. SLBF3463). 40 µg of proteins were mixed with the right amount of Laemmli Sample Buffer 4X (Bio-Rad), and boiled. Then samples were loaded on a 12% polyacrylamide-sodium dodecyl sulphate gel for SDS-PAGE. Proteins were transferred onto nitrocellulose membrane, using Mini Transfer Packs or Midi Transfer Packs, with Trans-Blot® Turbo ™ (Bio-Rad) according to manufacturer's instructions (Bio-Rad). The membranes were blocked in 5% skim milk (Sigma, Cat. 70166) for 45' at room temperature. Subsequently membranes were incubated with indicated primary antibody, overnight at 4°C. Primary antibodies used are listed in Table 1, anti- β-Actin was used to normalize protein loading.

Goat anti-mouse IgG (H+L) horseradish peroxidase-conjugated secondary antibody (Bio-Rad, 1:5000; Cat. 170-6516,) and Goat anti-rabbit Igg (H+L) horseradish peroxidase-conjugated secondary antibody (Bio-Rad, 1:5000; Cat. 170-6515,) were used as secondary antibodies. Detection was carried out with SuperSignal™ West Pico/femto PLUS Chemiluminescent Substrate (Thermo Scientific), based on the chemiluminescence of luminol and developed using ChemiDoc™ Imaging System (Bio-Rad). Full length uncropped original western blots used in their manuscript are provided as a single Supplemental Material file.

IHC. Ctr and 3xTg-AD mice were anesthetized with i.p. injection of Zoletil (80 mg/kg) and Xylazine (45 mg/kg) and intracardial perfused with cold PBS1x. Brains were dissected and sagittal sections were post-fixed in 4% paraformaldehyde in PBS1x. 40 µm slices were cut at microtome at -25°C and store at -20°C in 50% PBS1x, 25% ethylene- glycol and 25% glycerol. Free-floating staining of slices were performed. Briefly, slices were incubated with blocking solution, contains 10% serum, 1% BSA, 0,5% Triton X-100 in TBS1x, for 1 h at T room. Then, primary antibodies were applied o/n at 4°C in blocking solution. After 3 washes in TBS1x, slices were incubated with corresponding secondary antibodies for 1 h at T room, washed with TBS1x 3 times and then, counter-stained with DAPI. For co-staining, GFAP labelling was performed first and amplified with secondary antibodies plus streptavidin-Cy3 (Vector, cat. SA 1300). Then, other proteins detection was performed using corresponding primary antibodies (as p-eIF2α and GADD34) and secondary antibodies-488. Images were acquired using Leica SP8 LIGHTNING Confocal Microscope imaging systems. Images were acquired under non saturating conditions and analysed with Fiji ImageJ 1.52p software.

Primary antibodies used are anti- GFAP, Anti-p-eIF2α, Anti-Gadd 34 and Anti-Puromycin, indicated in *table 1*. Secondary antibodies are horse anti-goat biotinylated antibodies (Vector, cat. BA 9500), anti-mouse (Invitrogen, cat. A 11029) and anti-rabbit-488 antibodies (Invitrogen, cat. A32731).

Total RNA extraction and real-time PCR. Total mRNA was extracted from 1.0x10^6 cells using TRIzol Lysis Reagent (Invitrogel, Cat. 15596026) according to manufacturer's instruction. First strand of cDNA was synthesized from 0.5-1 µg of total RNA using Im-Prom-II system (Promega, Cat. A3800). Real-Time PCR

434 was performed using iTaq qPCR master mix according to manufacturer's instructions (Bio-Rad, Cat. 1725124)
435 on a SFX96 Real-time system (Bio-Rad). To normalize raw real time PCR data, S18 ribosomal subunit was
436 used. Data are expressed as delta-C (t) of gene of interest to S18 allowing appreciation of single gene
437 expression level. Oligonucleotide primers were as follows: Atf4 (NM_009716.3), forward:
438 GTTTAGAGCTAGGCAGTGAAG, reverse: CCTTTACACATGGAGGGATTAG; Xbp1 spliced (Xbp1s,
439 NM_001271730.1), forward: AGTCCGCAGCAGGTG, reverse: GGTCCAACTTGTCCAGAATG; Herpud1
440 (NM_022331.2), forward: GTGGAGGAAGATGATGAGATAAA, reverse:
441 CTCAGCGAGGAGTAGAAGTA; S18 (NM_011296), forward: TGCGAGTACTCAACACCAACA,
442 reverse: CTGCTTTCCTCAACACCACA

443

444 ***Proteomic analysis on astrocytes conditioned media.***

445 Astrocyte-conditioned media from WT-iAstro and 3Tg-iAstro cells, the cells treated with 4-PBA (3 µM, 48h)
446 or expressing 10nm-EML (8-10 ml from three independently plated 10 cm Petri dish per condition) were
447 collected, proteins were precipitated by TCA, washed and digested with trypsin. 100 µg of protein in 25 µl of
448 100 mM NH4HCO3 were reduced with 2.5 µL of 200 mM DTT (Sigma) at 90°C for 20 min and alkylated
449 with 10 µL 200 mM iodoacetamide (Sigma) for 1h at RT protected from light. Any excess of iodoacetamide
450 was removed by the addition of 200 mM DTT. The samples were then digested with 5 µg of trypsin (Promega,
451 Sequence Grade). After an ON incubation at 37°C, 2 µL of neat formic acid were added to stop trypsin activity
452 and the digested samples were dried by Speed Vacuum [79]. The peptide digests were desalted on the Discovery®
453 DSC-18 solid phase extraction (SPE) 96-well Plate (25 mg/well) (Sigma-Aldrich Inc., St. Louis, MO, USA)[80].

454 LC–MS/MS analyses were performed using a micro-LC Eksigent Technologies (Dublin, USA) system with a
455 stationary phase of a Halo Fused C18 column (0.5 × 100 mm, 2.7 µm; Eksigent Technologies, Dublin, USA).
456 The injection volume was 4.0 µL and the oven temperature was set at 40°C. The mobile phase was a mixture
457 of 0.1% (v/v) formic acid in water (A) and 0.1% (v/v) formic acid in acetonitrile (B), eluting at a flow-rate of
458 15.0 µL/min at increasing concentrations of B from 2% to 40% in 30 min. The LC system was interfaced with
459 a 5600+ TripleTOF system (AB Sciex, Concord, Canada) equipped with a DuoSpray Ion Source. Samples
460 were subjected to the traditional data-dependent acquisition (DDA) as previously described [81]. The MS data
461 were acquired with Analyst TF 1.7 (SCIEX, Concord, Canada). Three instrumental replicates for each sample
462 were subjected to the DIA analysis [82]. The MS files were searched using the software Mascot v. 2.4 (Matrix
463 Science Inc., Boston, USA) using trypsin as enzyme, with 2 missed cleavages and a search tolerance of 50
464 ppm was specified for the peptide mass tolerance, and 0.1 Da for the MS/MS tolerance, charges of the peptides
465 to search for were set to 2 +, 3 + and 4 +, and the search was set on monoisotopic mass and FDR at 1%. The
466 instrument was set to ESI-QUAD-TOF and the following modifications were specified for the search:
467 carbamidomethyl cysteines as fixed modification and oxidized methionine as variable modification. The
468 UniProt/Swiss-Prot reviewed database containing mouse proteins (version 12/10/2018, containing 25137
469 sequence entries) was used.

470 The quantification was performed by integrating the extracted ion chromatogram of all the unique ions for a
471 given peptide. The quantification was carried out with PeakView 2.0 and MarkerView 1.2. (Sciex, Concord,
472 ON, Canada). Six peptides per protein and six transitions per peptide were extracted from the SWATH files.
473 Shared peptides were excluded as well as peptides with modifications. Peptides with FDR lower than 1.0%
474 were exported in MarkerView for the t-test.
475
476 ***Statistical analysis.*** Statistical analysis and related graphical representations was done using GraphPad Prism
477 v.7. A two-tailed unpaired Student's t-test or one-way ANOVA test were used. No samples/results were
478 excluded from the analysis. Differences were considered significant at $p < 0.05$.
479

480 **LEGENDS**

481 **Figure 1. Protein synthesis analysis in WT- and 3Tg-iAstro cells. (a)** Cells were pulsed with puromycin (4
482 µM, 1.5 h), fixed and analysed by IF with anti-puromycin antibody (green) and with DAPI to stain nuclei
483 (blue). Images were acquired with Leica Thunder imager 3D live cell microscope, scale bar = 25 µm. Data are
484 expressed as mean ± SEM, WT-iAstro cells n = 40, 3Tg-iAstro cells n = 40, from 4 independent experiments;
485 ****, $p < 0.05$ by unpaired t test**. (b)** WB with anti-puromycin antibody and ponceau staining on cells treated
486 with 4 µM puromycin. Data are expressed as mean ± SEM of 12 independent experiments; ****, $p < 0.0001$
487 by unpaired t test**.**

488 **Figure 2. PERK-independent activation of p-eIF2α. (a)** Analysis of eIF2α phosphorylation and GADD34
489 expression on WT and 3Tg-iAstro. Cells were treated or not with 1 µM THG for 1 h, lysed and analysed by
490 WB with anti- p-eIF2α, eIF2α, GADD34 and actin antibodies. Data are expressed as mean ± SEM of n = 4
491 (3Tg-iAstro + THG), n = 5 (3Tg-iAstro) or n = 6 (WT- and WT-iAstro + THG) independent experiments; *,
492 $p < 0.05$ by one-way ANOVA, Sidak's multiple comparison; ***, $p<0.001$ Dunnet's multiple comparisons.
493 **(b)** Analysis of PERK phosphorylation and ATF4 induction on WT- and 3Tg-iAstro cells. WB analysis of
494 cells treated as in (a) with anti-p-PERK, PERK, ATF4 and actin antibodies. Data are expressed as mean ±
495 SEM from n = 3 (p-PERK and ATF) or n = 8 (PERK) independent experiments. *, $p < 0.05$, **, $p < 0.01$ and
496 ***, $p < 0.001$ by one-way ANOVA, Sidak's multiple comparison.

497 **Figure 3. ER stress/UPR genes induction in WT- and 3Tg-iAstro cells.** Real-time PCR of Atf4 **(a)**, Xbp1s
498 **(b)** and Herpud1 **(c)** transcripts in cells treated or not with 1 µM THG for 4h. Data of untreated WT- and 3Tg-
499 iAstro cells (middle plots) and THG treated /untreated cell (right plots) are presented separately. Values
500 represent mean ± SEM ΔC(t) of gene/S18 of 4 independent experiments for each condition. Left plots were
501 analyzed using ANOVA, with Tukey posthoc test; middle and right plots were analyzed using unpaired two-
502 tail Student's t-test.

503 **Figure 4. Forced ER-mitochondria interaction causes impairment of protein synthesis in WT-iAstro**
504 **cells.** WT-iAstro cells were non-transfected (WT Ctr) or transfected with mRFP (WT mRFP) and 10-nm ER-

505 mitochondrial linker (WT 10nm). **(a)** WB with anti-puromycin antibody and ponceau staining on lysates of
506 cells treated with 4 μM puromycin; data are expressed as mean ± SEM of 3 independent experiments; ***,
507 p<0.001 by one- way ANOVA, Sidak's multiple comparison. **(b)** WB analysis of eIF2α phosphorylation. Data
508 are expressed as mean ± SEM of 4 independent experiments; ****, p < 0.0001 by one- way ANOVA, Sidak's
509 multiple comparison. **(c)** Cells pulsed with 4 μM puromycin were fixed and analysed by IF with anti-
510 puromycin antibody (green). Images were acquired with Zeiss 710 confocal laser scanning microscope, data
511 are expressed as mean ± SEM of 3 independent coverslip; ***, p < 0.001 by unpaired t test. Scale bar = 25
512 μm. **(d)** Real-time PCR of Atf4, Xbp1s and Herpud1 transcripts in cells transfected with mRFP and 10-nm
513 ER-mitochondrial linker; data are expressed as mean ± SEM of 4 independent wells.

514 **Figure 5. Protein synthesis analysis in WT and 3xTg-AD mice.** WT and 3xTg-AD mice were i.p. injected
515 with 225 mg/Kg di puromycin and sacrificed 1.5 h post-injection. **(a)** WB with anti-puromycin, anti-actin
516 antibodies, and ponceau staining on hippocampal homogenates. Data are expressed as mean ± SEM of 13
517 independent WB from 2 mice per genotype. **, p < 0.01, unpaired t test. **(b)** IF with anti-puromycin antibody
518 (green) and DAPI (blue) of hippocampal brain slices. Data are expressed as mean ± SEM of 4 sections collected
519 from 2 mice per genotype. Scale bar = 50 μm.

520 **Figure 6. ER stress/UPR pathway in WT and 3xTg-AD mice. (a)** WB analysis with anti-PERK, p-eIF2α,
521 eIF2α, GADD34, ATF4 and actin on hippocampal homogenates of WT and 3xTg-AD (3xTg) mice. Data are
522 expressed as mean ± SEM of 6 independent experiments; *, p < 0.05; **, p < 0.01 by unpaired t test. **(b, c)**
523 Co-localization of p-eIF2α and GADD34 with GFAP and analysis on WT and 3xTg hippocampi. **(b)** IF on 40
524 μm thick brain slices with anti-GFAP (red), p-eIF2α (green) and DAPI (blue). Arrows indicate p-eIF2α-
525 expressing GFAP-positive astrocytes. **(c)** IF on 40 μm brain slices with anti-GFAP (red) and GADD34 (green)
526 and DAPI (blue). Images were acquire using Leica SP8 LIGHTNING Confocal Microscope imaging systems,
527 scale bar = 25μm. **(d)** qPCR of Atf4, Xbp1s and Herpud1 on the hippocampi of WT and 3xTg mice. Data are
528 expressed as mean ± SEM of 5-6 independent experiments, unpaired t test analysis.

529 **Figure 7. Compromised homeostatic functions of 3Tg-iAstro. (a)** ACM effects on neuronal protein
530 synthesis. Primary hippocampal neurons were treated with ACM from WT- or 3Tg-iAstro for 6 days (from
531 DIV6 to DIV12) and protein synthesis was evaluated treating cells with 4 μM puromycin for 1 h. IF images of
532 anti-puromycin staining (green) and DAPI (blue) were acquired with FV-1000 Olympus laser confocal
533 scanning system, scale bar = 30 μm. Data are expressed as mean ± SEM from n = 39 Ctr, n = 27 ACM WT-
534 iAstro, n = 34 ACM 3Tg-iAstro from 4 independent cultures; ***, p < 0.001 by one-way ANOVA Sidak's
535 multiple comparisons. **(b)** WB analysis with anti-puromycin, actin and ponceau staining of neuronal lysates
536 treated as in (a). Data are expressed as mean ± SEM from n = 8 (Ctr) or n = 5 (ACM WT and ACM 3Tg)
537 independent experiments; **, p < 0.01 by one-way ANOVA, Sidak's multiple comparisons. **(c)** WB analysis
538 with anti-puromycin and ponceau staining of neuronal lysates treated or not with ACM from WT-iAstro or
539 WT-iAstro expressing 10nm-EML. Data are expressed as mean ± SEM of 4 independent experiments; ***, p
540 < 0.001 by one-way ANOVA, Sidak's multiple comparisons. **(d)** Co-culture of pericytes and endothelial cells

541 (EC) with either WT-iAstro (P/EC/WT-iAstro) or 3Tg-iAstro (P/EC/3Tg-iAstro)) or WT-iAstro expressing
542 the 10nm-EML (P/EC/WT-iAstro+10nm) cells on a layer of Matrigel. Images were acquired by Zeiss 710
543 confocal laser scanning microscope, scale bar = 500 μm. Data are expressed as mean ± SEM of n = 3 (WT-
544 RFP and 3Tg-RFP) or n = 6 (WT-10nm) independent experiments; ***, $p < 0.001$, ****, $p < 0.0001$, by one-
545 way ANOVA Sidak's multiple comparisons.

546 **Figure 8. Proteomic analysis of WT- and 3Tg-iAstro secretome.** ACM (10 ml) was collected from 48 h
547 culture of WT-iAstro, 3Tg-iAstro and 3Tg-iAstro cells treated with 4-PBA (3 μM, 48h). Proteins were
548 precipitated by TCA and processed as described in Methods section. 120, 84 and 102 proteins were identified
549 in WT-iAstro, 3Tg-iAstro and 3Tg-iAstro + 4-PBA ACM, respectively. Protein quantification of 3Tg-iAstro
550 vs WT-iAstro ACM returned five differentially regulated proteins (1.3 fold change cut-off, $p < 0.05$) (left
551 upper table). Gene ontology analysis of proteins, unique for WT-iAstro or 3Tg-iAstro + 4-PBA both compared
552 with 3Tg-iAstro ACM, returned GO terms related to extracellular matrix, focal adhesion and cadherin binding
553 overrepresented in both WT-iAstro and 3Tg-iAstro + 4-PBA, but not in 3Tg-iAstro cells (right bottom table).

554 **Figure 9. 4-PBA rescues protein synthesis and p-eIF2α in 3Tg i-Astro and tubulogenesis in pericyte/EC**
555 **co-cultures. (a)** WT- and Tg-iAstro were treated or not with 4-PBA 3μM, for 48h, cells were pulsed with
556 puromycin 4 μM and analysed by WB with anti-puromycin antibody and ponceau staining. Data are
557 expressed as mean ± SEM from 6-4 independent experiments; **, $p < 0.01$; ***, $p < 0.001$, one-way ANOVA,
558 Sidak's multiple comparisons. **(b)** WB analysis of eIF2α phosphorylation on WT-iAstro and 3Tg-iAstro,
559 treated or not with 4-PBA 3 μM, for 48h. Data are expressed as mean ± SEM from 4 independent experiments;
560 **, $p < 0.01$, one-way ANOVA, Sidak's multiple comparisons. **(c)** Representative images and quantification
561 of SPLICS fluorescence, indicating ER-mitochondrial contacts at ∼8–10 nm distance, in WT-iAstro, 3Tg-
562 iAstro, and in 3Tg-iAstro treated with 4-PBA (3μM, for 48h). Data are expressed as mean ± SEM of n = 22
563 (WT-iAstro), n = 30 (Tg-iAstro), n=32 (Tg-iAstro + 4-PBA), from 3 independent coverslip , ****, $p < 0.0001$,
564 one-way ANOVA, Sidak's multiple comparisons. Scale bar = 20 μM. **(d)** Co-cultures of pericytes, endothelial
565 cells and WT-iAstro or 3Tg-iAstro (pre-treated or not with 4-PBA for 48 h) were plated in a layer of Matrigel
566 in presence or absence of 4-PBA (3μM). After 8 h, bright field images were taken using a Zeiss 710 confocal
567 laser scanning microscope, scale bar = 500 μm. Data are expressed as mean ± SEM, n = 4 from 2 independent
568 experiments; ***, $p < 0.001$ by one-way ANOVA, Sidak's multiple comparisons.

569 **Figure 10. Schematic representation of the role of impaired proteins synthesis in the loss of homeostatic**
570 **functions by AD astrocytes.** Phosphorylation of eIF2α and reduction of protein synthesis in AD astrocytes
571 occurs without induction of overt ER stress/UPR and activation of PERK (∼ ER stress, ∼ PERK and
572 intermittent red line). A role of PKR, HRI and GCN2 kinases is to be determined (blue arrow and question
573 mark). Alteration of ER-mitochondrial interaction could be a plausible candidate (10 nm, red arrowheads and
574 red thick arrow), as well as a reduced ATP supply by mitochondria (curved red arrow). A role of protein
575 misfolding and ER Ca^{2+} dyshomeostasis is hypothesized (? Misfolding, ? ER Ca^{2+}). The deregulation of
576 proteins synthesis may potentially result in impaired secretion (red intermittent arrows) of neurotrophic and

577 neuroprotective molecules as well as impaired formation of extracellular matrix (SPARC, heat shock proteins
578 (HSPs), Adhesion, ECM). Protein synthesis, p-eIF2α levels and homeostatic functions can be rescued by the
579 chemical chaperone 4-PBA (green arrows).

580

581 **Author contribution.**

582 Conceptualization and data interpretation A.A.Genazzani, D.L. and L.T.; methodology, G.D., E.R., M.
583 Manfredi, M.C., E.DG., A.G. and M.G.; software, M.G. and M. Manfredi; validation, M. Moro, B.P.,
584 E.T.,V.V.V., D.G., A. LF., E.B., S.V., G.D. and E.R.; formal analysis, M. Moro, G.D., E.R., M. Manfredi, D.L
585 and L.T.; investigation, G.D., E.R., V.V.V., A.A.Grolla, M. Moro, D.L and L.T.; resources, A.A.Grolla, M.C.,
586 M. Manfredi, M.G. and E.DG.; data curation, V.V.V., M. Moro, G.D. and L.T; writing—original draft
587 preparation, M. Moro, G.D., L.T and D.L.; writing—review and editing, G.D., L.T., D.L., A.A.Grolla,
588 A.A.Genazzani; supervision, L.T., D.L. and A.A.Genazzani; project administration, L.T., A.A.Genazzani and
589 D.L.; funding acquisition, M. Manfredi, A.A.Genazzani, and D.L. All authors have read and agreed to the
590 published version of the manuscript.

591 **Conflict of interest.** The authors declare that they have no conflict of interest

592 **Funding.** This work had the following financial supports: grants 2013-0795 to AAG, 2014-1094 to D.L. from
593 the Fondazione Cariplo; grants FAR-2016 and FAR-2019 to D.L. from The Università del Piemonte Orientale;
594 partially funded by the AGING Project – Department of Excellence – DIMET, Università del Piemonte
595 Orientale to M.Manfredi; L.T. was supported by fellowship from the CRT Foundation (1393-2017).

596 **Acknowledgment.** Advance imaging System-CAAD**-** Center for Translational Research on Autoimmune and
597 Allergic Disease-Università del Piemonte Orientale "Amedeo Avogadro", Novara, Italy. We thank Drs György
598 Csordás and György Hajnóczky (Thomas Jefferson University) for kind donation of 10 nm ER-mitochondrial
599 linker.

600 **REFERENCES**

601 1 Muneer A, Shamsher Khan RM. Endoplasmic Reticulum Stress: Implications for Neuropsychiatric
602 Disorders. *Chonnam Med J* 2019; **55**: 8–19.

603 2 Scheper W, Hoozemans JJM. The unfolded protein response in neurodegenerative diseases: a
604 neuropathological perspective. *Acta Neuropathol* 2015; **130**: 315–331.

605 3 Halliday M, Radford H, Zents KAM, Molloy C, Moreno JA, Verity NC *et al.* Repurposed drugs targeting
606 eIF2α-P-mediated translational repression prevent neurodegeneration in mice. *Brain* 2017; **140**:
607 1768–1783.

608 4 Garcia-Esparcia P, Sideris-Lampretsas G, Hernandez-Ortega K, Grau-Rivera O, Sklaviadis T, Gelpi E *et al.*
609 Altered mechanisms of protein synthesis in frontal cortex in Alzheimer disease and a mouse model. *Am*
610 *J Neurodegener Dis* 2017; **6**: 15–25.

611 5 Buchanan H, Mackay M, Palmer K, Tothová K, Katsur M, Platt B *et al.* Synaptic Loss, ER Stress and
612 Neuro-Inflammation Emerge Late in the Lateral Temporal Cortex and Associate with Progressive Tau
613 Pathology in Alzheimer's Disease. *Mol Neurobiol* 2020; **57**: 3258–3272.

614 6 Duran-Aniotz C, Cornejo VH, Espinoza S, Ardiles ÁO, Medinas DB, Salazar C *et al.* IRE1 signaling
615 exacerbates Alzheimer's disease pathogenesis. *Acta Neuropathol* 2017; **134**: 489–506.

616 7 Ma T, Trinh MA, Wexler AJ, Bourbon C, Gatti E, Pierre P *et al.* Suppression of eIF2α kinases alleviates
617 Alzheimer's disease-related plasticity and memory deficits. *Nat Neurosci* 2013; **16**: 1299–1305.

618 8 Hashimoto S, Saido TC. Critical review: involvement of endoplasmic reticulum stress in the aetiology of
619 Alzheimer's disease. *Open Biol* 2018; **8**. doi:10.1098/rsob.180024.

620 9 Pakos-Zebrucka K, Koryga I, Mnich K, Ljujic M, Samali A, Gorman AM. The integrated stress response.
621 *EMBO Rep* 2016; **17**: 1374–1395.

622 10 Costa-Mattioli M, Walter P. The integrated stress response: From mechanism to disease. *Science* 2020;
623 **368**: eaat5314.

624 11 Hetz C, Zhang K, Kaufman RJ. Mechanisms, regulation and functions of the unfolded protein response.
625 *Nat Rev Mol Cell Biol* 2020; **21**: 421–438.

626 12 Kumar V, Maity S. ER Stress-Sensor Proteins and ER-Mitochondrial Crosstalk-Signaling Beyond (ER)
627 Stress Response. *Biomolecules* 2021; **11**: 173.

628 13 Semyanov A, Verkhratsky A. Astrocytic processes: from tripartite synapses to the active milieu. *Trends*
629 *Neurosci* 2021; **44**: 781–792.

630 14 Sakers K, Lake AM, Khazanchi R, Ouwenga R, Vasek MJ, Dani A *et al.* Astrocytes locally translate
631 transcripts in their peripheral processes. *Proc Natl Acad Sci U S A* 2017; **114**: E3830–E3838.

632 15 Boulay A-C, Saubaméa B, Adam N, Chasseigneaux S, Mazaré N, Gilbert A *et al.* Translation in astrocyte
633 distal processes sets molecular heterogeneity at the gliovascular interface. *Cell Discov* 2017; **3**: 17005.

634 16 Sims SG, Cisney RN, Lipscomb MM, Meares GP. The role of endoplasmic reticulum stress in astrocytes.
635 *Glia* 2022; **70**: 5–19.

636 17 Lim D, Iyer A, Ronco V, Grolla AA, Canonico PL, Aronica E *et al.* Amyloid beta deregulates astroglial
637 mGluR5-mediated calcium signaling via calcineurin and Nf-kB. *Glia* 2013; **61**: 1134–1145.

638 18 Ruffinatti F, Tapella L, Gregnanin I, Stevano A, Chiorino G, Canonico PL *et al.* Transcriptional remodeling
639 in primary hippocampal astrocytes from an Alzheimer's disease mouse model. *CURRENT ALZHEIMER*
640 *RESEARCH* 2018; **15**. doi:10.2174/1567205015666180613113924.

641 19 Rocchio Francesca, Tapella Laura, Manfredi Marcello, Chisari Mariangela, Ronco Francesca, Ruffinatti
642 Federico Alessandro *et al.* Gene expression, proteome and calcium signaling alterations in immortalized
643 hippocampal astrocytes from an Alzheimer's disease mouse model. *CELL DEATH & DISEASE* 2019; **10**:
644 24.

645 20 Dematteis G, Vydmantaitė G, Ruffinatti FA, Chahin M, Farruggio S, Barberis E *et al.* Proteomic analysis
646 links alterations of bioenergetics, mitochondria-ER interactions and proteostasis in hippocampal
647 astrocytes from 3xTg-AD mice. *Cell Death Dis* 2020; **11**: 645.

648 21 Lim D, Dematteis G, Tapella L, Genazzani AA, Calì T, Brini M *et al.* Ca2+ handling at the mitochondria-ER
649 contact sites in neurodegeneration. *Cell Calcium* 2021; **98**: 102453.

650 22 Dematteis G., Restelli E., Chiesa R., Aronica E., Genazzani A. A., Lim D. *et al.* Calcineurin controls
651 expression of EAAT1/GLAST in mouse and human cultured astrocytes through dynamic regulation of
652 protein synthesis and degradation. *INTERNATIONAL JOURNAL OF MOLECULAR SCIENCES* 2020; **21**:
653 2213.

654 23 Dematteis G, Restelli E, Vanella VV, Manfredi M, Marengo E, Corazzari M *et al.* Calcineurin Controls
655 Cellular Prion Protein Expression in Mouse Astrocytes. *Cells* 2022; **11**: 609.

656 24 Cieri D, Vicario M, Giacomello M, Vallese F, Filadi R, Wagner T *et al.* SPLICS: a split green fluorescent
657 protein-based contact site sensor for narrow and wide heterotypic organelle juxtaposition. *Cell Death*
658 *Differ* 2018; **25**: 1131–1145.

659 25 Vallese F, Catoni C, Cieri D, Barazzuol L, Ramirez O, Calore V *et al.* An expanded palette of improved
660 SPLICS reporters detects multiple organelle contacts in vitro and in vivo. *Nat Commun* 2020; **11**: 6069.

661 26 Calì T, Brini M. Quantification of organelle contact sites by split-GFP-based contact site sensors (SPLICS)
662 in living cells. *Nat Protoc* 2021; **16**: 5287–5308.

663 27 Csordás G, Renken C, Várnai P, Walter L, Weaver D, Buttle KF *et al.* Structural and functional features
664 and significance of the physical linkage between ER and mitochondria. *J Cell Biol* 2006; **174**: 915–921.

665 28 Ding Q, Markesbery WR, Chen Q, Li F, Keller JN. Ribosome Dysfunction Is an Early Event in Alzheimer's
666 Disease. *J Neurosci* 2005; **25**: 9171–9175.

667 29 Ma T. Dysregulation of Neuronal Protein Synthesis in Alzheimer's Disease. The Oxford Handbook of
668 Neuronal Protein Synthesis. 2021. doi:10.1093/oxfordhb/9780190686307.013.18.

669 30 Santini E, Huynh TN, Klann E. Mechanisms of Translation Control Underlying Long-lasting Synaptic
670 Plasticity and the Consolidation of Long-term Memory. *Prog Mol Biol Transl Sci* 2014; **122**: 131–167.

671 31 Rosenberg T, Gal-Ben-Ari S, Dieterich DC, Kreutz MR, Ziv NE, Gundelfinger ED *et al.* The roles of protein
672 expression in synaptic plasticity and memory consolidation. *Frontiers in Molecular Neuroscience* 2014;
673 **7**.https://www.frontiersin.org/article/10.3389/fnmol.2014.00086 (accessed 1 Feb2022).

674 32 Kucukdereli H, Allen NJ, Lee AT, Feng A, Ozlu MI, Conatser LM *et al.* Control of excitatory CNS
675 synaptogenesis by astrocyte-secreted proteins Hevin and SPARC. *PNAS* 2011; **108**: E440–E449.

676 33 Lyon MS, Milligan C. Extracellular heat shock proteins in neurodegenerative diseases: New
677 perspectives. *Neurosci Lett* 2019; **711**: 134462.

678 34 Calderwood SK, Borges TJ, Eguchi T, Lang BJ, Murshid A, Okusha Y *et al.* Extracellular Hsp90 and
679 protection of neuronal cells through Nrf2. *Biochem Soc Trans* 2021; **49**: 2299–2306.

680 35 Cuadrado-Tejedor M, García-Osta A, Ricobaraza A, Oyarzabal J, Franco R. Defining the mechanism of
681 action of 4-phenylbutyrate to develop a small-molecule-based therapy for Alzheimer's disease. *Curr*
682 *Med Chem* 2011; **18**: 5545–5553.

683 36 Cuadrado-Tejedor M, Ricobaraza AL, Torrijo R, Franco R, Garcia-Osta A. Phenylbutyrate is a
684 multifaceted drug that exerts neuroprotective effects and reverses the Alzheimer´s disease-like
685 phenotype of a commonly used mouse model. *Curr Pharm Des* 2013; **19**: 5076–5084.

686 37 Groenendyk J, Agellon LB, Michalak M. Calcium signaling and endoplasmic reticulum stress. In:
687 *International Review of Cell and Molecular Biology*. Academic Press, 2021
688 doi:10.1016/bs.ircmb.2021.03.003.

689 38 Bullido MJ, Martínez-García A, Tenorio R, Sastre I, Muñoz DG, Frank A *et al.* Double stranded RNA
690 activated EIF2 alpha kinase (EIF2AK2; PKR) is associated with Alzheimer's disease. *Neurobiol Aging*
691 2008; **29**: 1160–1166.

692 39 Moradi Majd R, Mayeli M, Rahmani F. Pathogenesis and promising therapeutics of Alzheimer disease
693 through eIF2α pathway and correspondent kinases. *Metab Brain Dis* 2020; **35**: 1241–1250.

694 40 Hugon J, Paquet C. The PKR/P38/RIPK1 Signaling Pathway as a Therapeutic Target in Alzheimer's
695 Disease. *Int J Mol Sci* 2021; **22**: 3136.

696 41 Area-Gomez E, Schon EA. On the Pathogenesis of Alzheimer's Disease: The MAM Hypothesis. *FASEB J*
697 2017; **31**: 864–867.

698 42 Paillusson S, Stoica R, Gomez-Suaga P, Lau DHW, Mueller S, Miller T *et al.* There's Something Wrong
699 with my MAM; the ER-Mitochondria Axis and Neurodegenerative Diseases. *Trends Neurosci* 2016; **39**:
700 146–157.

701 43 Lim D, Ronco V, Grolla AA, Verkhratsky A, Genazzani AA. Glial calcium signalling in Alzheimer's disease.
702 *Rev Physiol Biochem Pharmacol* 2014; **167**: 45–65.

703 44 Lim D, Rodríguez-Arellano JJ, Parpura V, Zorec R, Zeidán-Chuliá F, Genazzani AA *et al.* Calcium signalling
704 toolkits in astrocytes and spatio-temporal progression of Alzheimer's disease. *Curr Alzheimer Res* 2016;
705 **13**: 359–369.

706 45 Lim D, Semyanov A, Genazzani A, Verkhratsky A. Calcium signaling in neuroglia. In: *International Review*
707 *of Cell and Molecular Biology*. Academic Press, 2021 doi:10.1016/bs.ircmb.2021.01.003.

708 46 De Strooper B, Karran E. The Cellular Phase of Alzheimer's Disease. *Cell* 2016; **164**: 603–615.

709 47 Hipp MS, Kasturi P, Hartl FU. The proteostasis network and its decline in ageing. *Nat Rev Mol Cell Biol*
710 2019; **20**: 421–435.

711 48 Kurtishi A, Rosen B, Patil KS, Alves GW, Møller SG. Cellular Proteostasis in Neurodegeneration. *Mol*
712 *Neurobiol* 2019; **56**: 3676–3689.

713 49 Griffiths EJ, Rutter GA. Mitochondrial calcium as a key regulator of mitochondrial ATP production in
714 mammalian cells. *Biochim Biophys Acta* 2009; **1787**: 1324–1333.

715 50 Bier DM. *The Energy Costs of Protein Metabolism: Lean and Mean on Uncle Sam's Team*. National
716 Academies Press (US), 1999https://www.ncbi.nlm.nih.gov/books/NBK224633/ (accessed 29 Jan2022).

717 51 Qiao J, Wang J, Wang H, Zhang Y, Zhu S, Adilijiang A *et al.* Regulation of astrocyte pathology by
718 fluoxetine prevents the deterioration of Alzheimer phenotypes in an APP/PS1 mouse model. *Glia* 2016;
719 **64**: 240–254.

720 52 TAPELLA LAURA PAOLA FERILDE, Cerruti Matteo, Biocotino Isabella, STEVANO ALESSIO, Rocchio
721 Francesca, Canonico Pier Luigi *et al.* TGF-β2 and TGF-β3 from cultured β-amyloid-treated or 3xTg-AD-
722 derived astrocytes may mediate astrocyte-neuron communication. *EUROPEAN JOURNAL OF*
723 *NEUROSCIENCE* 2018; **47**: 211–221.

724 53 Zhong N, Ramaswamy G, Weisgraber KH. Apolipoprotein E4 domain interaction induces endoplasmic
725 reticulum stress and impairs astrocyte function. *J Biol Chem* 2009; **284**: 27273–27280.

726 54 Cvijetic S, Bortolotto V, Manfredi M, Ranzato E, Marengo E, Salem R *et al.* Cell autonomous and
727 noncell-autonomous role of NF-κB p50 in astrocyte-mediated fate specification of adult neural
728 progenitor cells. *Glia* 2017; **65**: 169–181.

729 55 Risher WC, Kim N, Koh S, Choi J-E, Mitev P, Spence EF *et al.* Thrombospondin receptor α2δ-1 promotes
730 synaptogenesis and spinogenesis via postsynaptic Rac1. *J Cell Biol* 2018; **217**: 3747–3765.

731 56 Chaplot K, Jarvela TS, Lindberg I. Secreted Chaperones in Neurodegeneration. *Front Aging Neurosci*
732 2020; **12**: 268.

733 57 Lackie RE, Maciejewski A, Ostapchenko VG, Marques-Lopes J, Choy W-Y, Duennwald ML *et al.* The
734 Hsp70/Hsp90 Chaperone Machinery in Neurodegenerative Diseases. *Front Neurosci* 2017; **11**: 254.

735 58 Upadhya R, Zingg W, Shetty S, Shetty AK. Astrocyte-derived extracellular vesicles: Neuroreparative
736 properties and role in the pathogenesis of neurodegenerative disorders. *J Control Release* 2020; **323**:
737 225–239.

738 59 Baeten KM, Akassoglou K. Extracellular matrix and matrix receptors in blood-brain barrier formation
739 and stroke. *Dev Neurobiol* 2011; **71**: 1018–1039.

740 60 Benarroch EE. Extracellular matrix in the CNS: Dynamic structure and clinical correlations. *Neurology*
741 2015; **85**: 1417–1427.

742 61 Wiese S, Karus M, Faissner A. Astrocytes as a source for extracellular matrix molecules and cytokines.
743 *Front Pharmacol* 2012; **3**: 120.

744 62 Corazzari M, Rapino F, Ciccosanti F, Giglio P, Antonioli M, Conti B *et al.* Oncogenic BRAF induces chronic
745 ER stress condition resulting in increased basal autophagy and apoptotic resistance of cutaneous
746 melanoma. *Cell Death Differ* 2015; **22**: 946–958.

747 63 Giglio P, Gagliardi M, Tumino N, Antunes F, Smaili S, Cotella D *et al.* PKR and GCN2 stress kinases
748 promote an ER stress-independent eIF2α phosphorylation responsible for calreticulin exposure in
749 melanoma cells. *Oncoimmunology* 2018; **7**: e1466765.

750 64 Kolb PS, Ayaub EA, Zhou W, Yum V, Dickhout JG, Ask K. The therapeutic effects of 4-phenylbutyric acid
751 in maintaining proteostasis. *Int J Biochem Cell Biol* 2015; **61**: 45–52.

752 65 Lebeau PF, Platko K, Byun JH, Austin RC. Calcium as a reliable marker for the quantitative assessment of
753 endoplasmic reticulum stress in live cells. *J Biol Chem* 2021; **296**: 100779.

754 66 Lin H, Peng Y, Li J, Wang Z, Chen S, Qing X *et al.* Reactive Oxygen Species Regulate Endoplasmic
755 Reticulum Stress and ER-Mitochondrial Ca2+ Crosstalk to Promote Programmed Necrosis of Rat
756 Nucleus Pulposus Cells under Compression. *Oxid Med Cell Longev* 2021; **2021**: 8810698.

757 67 Malo A, Krüger B, Göke B, Kubisch CH. 4-Phenylbutyric acid reduces endoplasmic reticulum stress,
758 trypsin activation, and acinar cell apoptosis while increasing secretion in rat pancreatic acini. *Pancreas*
759 2013; **42**: 92–101.

760 68 Zhong Y, Jin C, Han J, Zhu J, Liu Q, Sun D *et al.* Inhibition of ER stress attenuates kidney injury and
761 apoptosis induced by 3-MCPD via regulating mitochondrial fission/fusion and Ca2+ homeostasis. *Cell*
762 *Biol Toxicol* 2021; **37**: 795–809.

763 69 Sharma M, Naura AS, Singla SK. A deleterious interplay between endoplasmic reticulum stress and its
764 functional linkage to mitochondria in nephrolithiasis. *Free Radic Biol Med* 2021; **168**: 70–80.

765 70 Cuadrado-Tejedor M, García-Osta A, Ricobaraza A, Oyarzabal J, Franco R. Defining the mechanism of
766 action of 4-phenylbutyrate to develop a small-molecule-based therapy for Alzheimer's disease. *Curr*
767 *Med Chem* 2011; **18**: 5545–5553.

768 71 Gerakis Y, Hetz C. Emerging roles of ER stress in the etiology and pathogenesis of Alzheimer's disease.
769 *FEBS J* 2018; **285**: 995–1011.

770 72 Remondelli P, Renna M. The Endoplasmic Reticulum Unfolded Protein Response in Neurodegenerative
771 Disorders and Its Potential Therapeutic Significance. *Front Mol Neurosci* 2017; **10**: 187.

772 73 Rozpedek W, Markiewicz L, Diehl JA, Pytel D, Majsterek I. Unfolded Protein Response and PERK Kinase
773 as a New Therapeutic Target in the Pathogenesis of Alzheimer's Disease. *Curr Med Chem* 2015; **22**:
774 3169–3184.

775 74 Singh R, Kaur N, Dhingra N, Kaur T. Protein misfolding, ER Stress and Chaperones: An approach to
776 develop chaperone-based therapeutics for Alzheimer's Disease. *Int J Neurosci* 2021; : 1–32.

777 75 Laura Tapella, Teresa Soda, Lisa Mapelli, Valeria Bortolotto, Heather Bondi, Federico A. Ruffinatti *et al.*
778 Deletion of calcineurin from GFAP-expressing astrocytes impairs excitability of cerebellar and
779 hippocampal neurons through astroglial Na+ /K+ ATPase. *GLIA* 2019. doi:10.1002/glia.23737.

780 76 Ozcan U, Yilmaz E, Ozcan L, Furuhashi M, Vaillancourt E, Smith RO *et al.* Chemical chaperones reduce
781 ER stress and restore glucose homeostasis in a mouse model of type 2 diabetes. *Science* 2006; **313**:
782 1137–1140.

783 77 Schmidt EK, Clavarino G, Ceppi M, Pierre P. SUnSET, a nonradioactive method to monitor protein
784 synthesis. *Nat Methods* 2009; **6**: 275–277.

785 78 Koren SA, Hamm MJ, Meier SE, Weiss BE, Nation GK, Chishti EA *et al.* Tau drives translational selectivity
786 by interacting with ribosomal proteins. *Acta Neuropathol* 2019; **137**: 571–583.

787 79 Dalla Pozza E, Manfredi M, Brandi J, Buzzi A, Conte E, Pacchiana R *et al.* Trichostatin A alters
788 cytoskeleton and energy metabolism of pancreatic adenocarcinoma cells: An in depth proteomic study.
789 *J Cell Biochem* 2018; **119**: 2696–2707.

790 80 Manfredi M, Robotti E, Bearman G, France F, Barberis E, Shor P *et al.* Direct Analysis in Real Time Mass
791 Spectrometry for the Nondestructive Investigation of Conservation Treatments of Cultural Heritage. *J*
792 *Anal Methods Chem* 2016; **2016**: 6853591.

793 81 Manfredi M, Martinotti S, Gosetti F, Ranzato E, Marengo E. The secretome signature of malignant
794 mesothelioma cell lines. *J Proteomics* 2016; **145**: 3–10.

795 82 Manfredi M, Brandi J, Di Carlo C, Vita Vanella V, Barberis E, Marengo E *et al.* Mining cancer biology
796 through bioinformatic analysis of proteomic data. *Expert Rev Proteomics* 2019; **16**: 733–747.

797

798

799 ***Table1***. List of primary antibodies.

Primary antibody	Dilition WB	Dilution ICC/IHC	Cat. N.	House
Anti-ATF 4	1:500		390063	Santa Cruz
Anti-eIF2α	1:500		133132	Santa Cruz
Anti-p-eIF2α	1:500	1:200	ABP-0745	Immunological Sciences
Anti-Gadd 34	1:550	1:100	OTI2B11	Abcam
Anti-GFAP		1:100	MAB-12029	Immunological Sciences
Anti-PERK	1:500		C33E10	Cell Signaling Technology
Anti-p-PERK	1:500		16F8	Cell Signaling Technology
Anti-Puromycin	1:1000	1:200	MABE343	Millipore
Anti-β-actin	1:2000		A1978	Sigma Aldrich

800

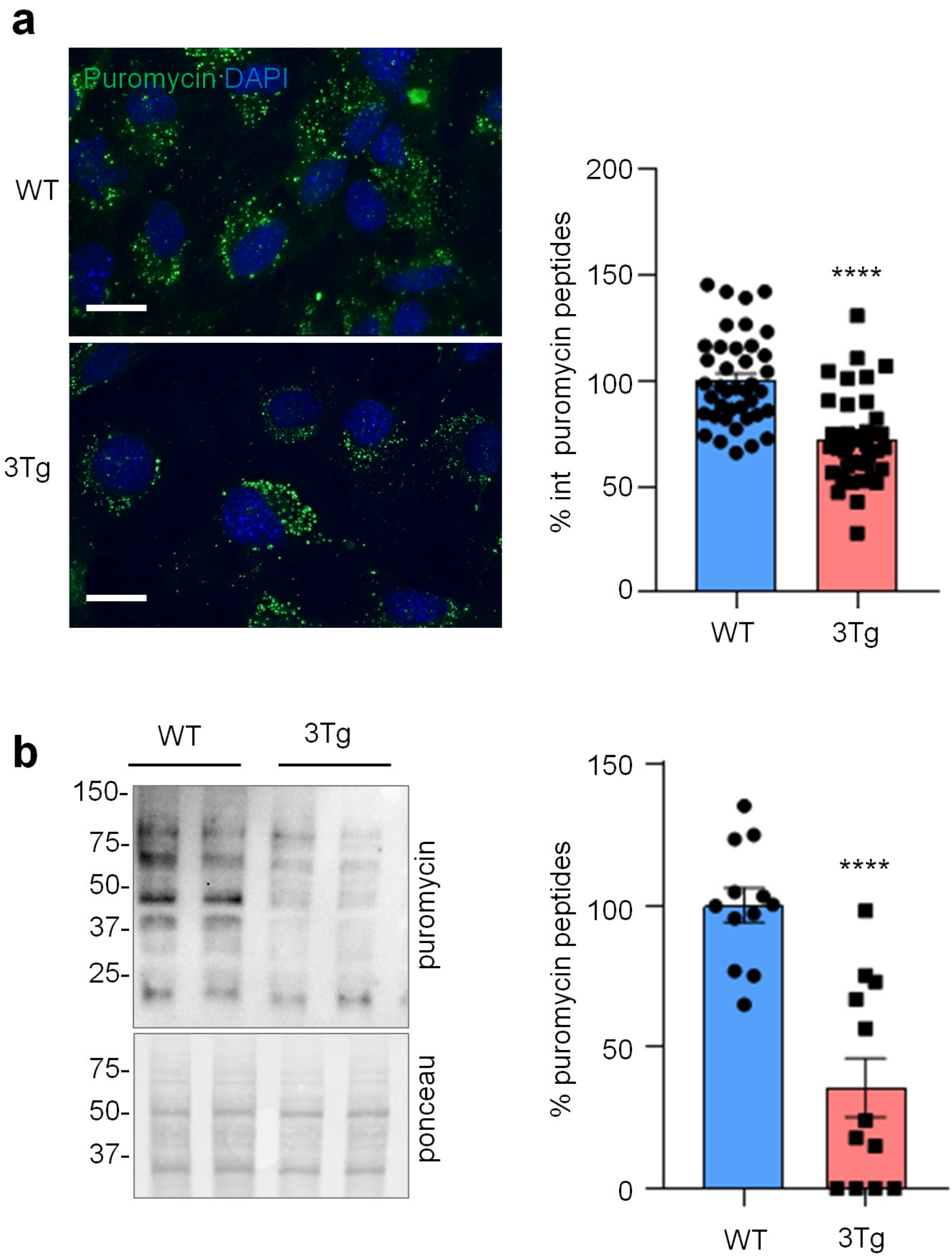
a
Puromycin DAPI
WT
3Tg
% int puromycin peptides
200
150
100
50
0
****
WT
3Tg
b
WT
3Tg
150-
75-
50-
37-
25-
puromycin
75-
50-
37-
ponceau
% puromycin peptides
150
100
50
0
****
WT
3Tg

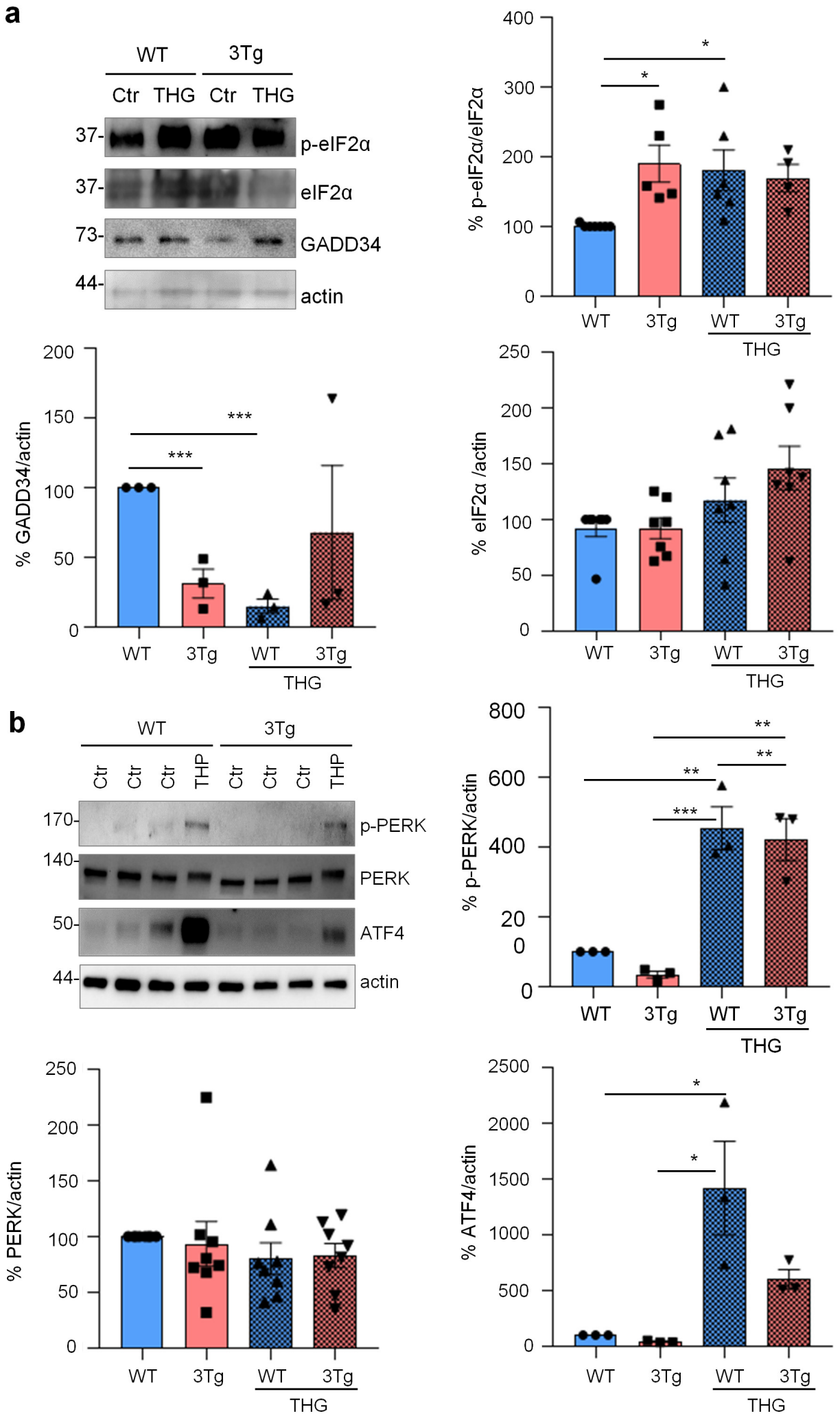
a
WT
3Tg
Ctr
THG
Ctr
THG
37-
p-eIF2α
37-
eIF2α
73-
GADD34
44-
actin
% p-eIF2α/eIF2α
% GADD34/actin
% eIF2α /actin
WT
3Tg
WT
3Tg
THG
b
WT
3Tg
Ctr
Ctr
Ctr
THP
Ctr
Ctr
Ctr
THP
170-
p-PERK
140-
PERK
50-
ATF4
44-
actin
% p-PERK/actin
% PERK/actin
% ATF4/actin

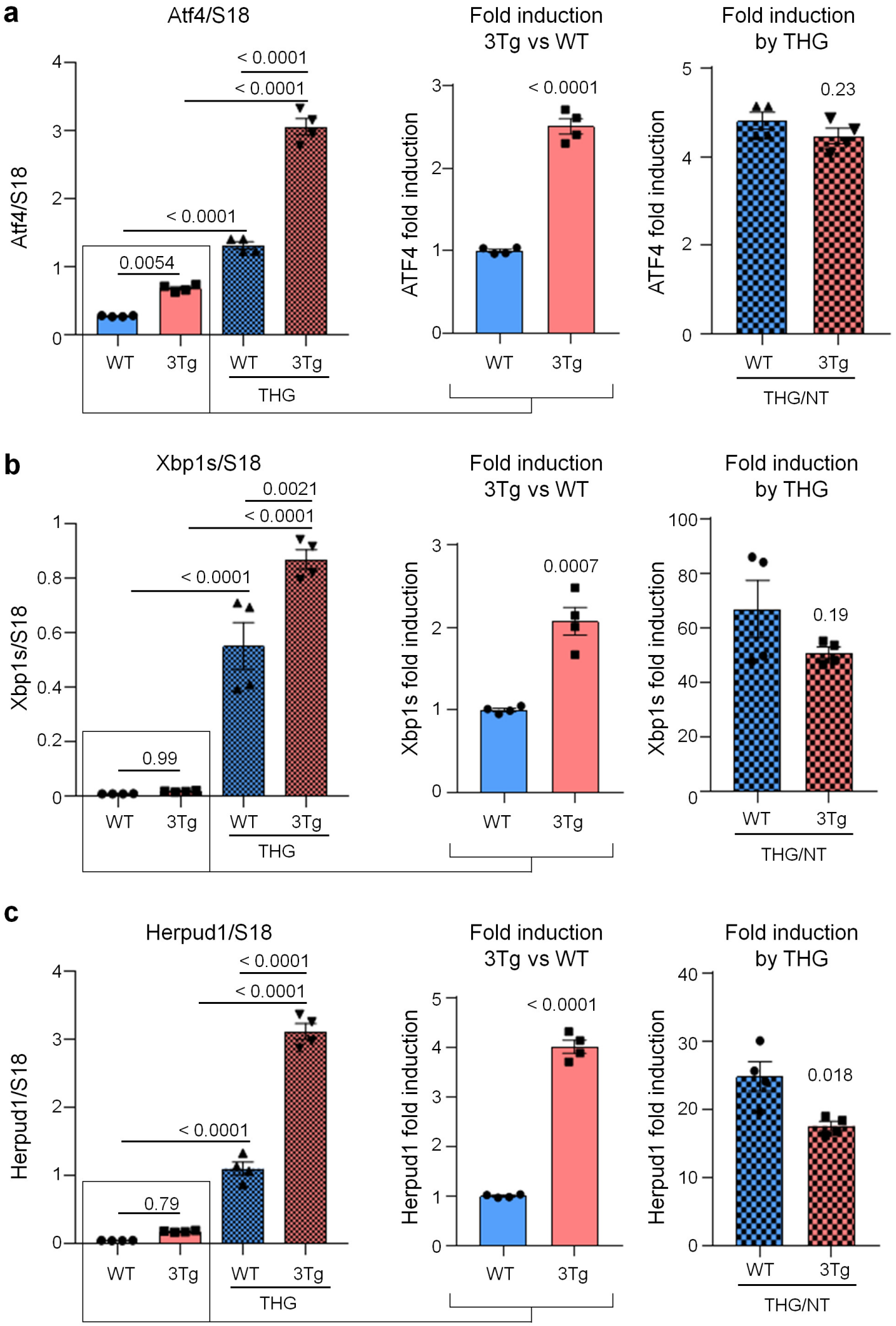
a
Atf4/S18
Atf4/S18
< 0.0001
< 0.0001
< 0.0001
0.0054
WT
3Tg
WT
3Tg
THG
Fold induction
3Tg vs WT
ATF4 fold induction
< 0.0001
WT
3Tg
Fold induction
by THG
ATF4 fold induction
0.23
WT
3Tg
THG/NT
b
Xbp1s/S18
Xbp1s/S18
0.0021
< 0.0001
< 0.0001
0.99
WT
3Tg
WT
3Tg
THG
Fold induction
3Tg vs WT
Xbp1s fold induction
0.0007
WT
3Tg
Fold induction
by THG
Xbp1s fold induction
0.19
WT
3Tg
THG/NT
c
Herpud1/S18
Herpud1/S18
< 0.0001
< 0.0001
< 0.0001
0.79
WT
3Tg
WT
3Tg
THG
Fold induction
3Tg vs WT
Herpud1 fold induction
< 0.0001
WT
3Tg
Fold induction
by THG
Herpud1 fold induction
0.018
WT
3Tg
THG/NT

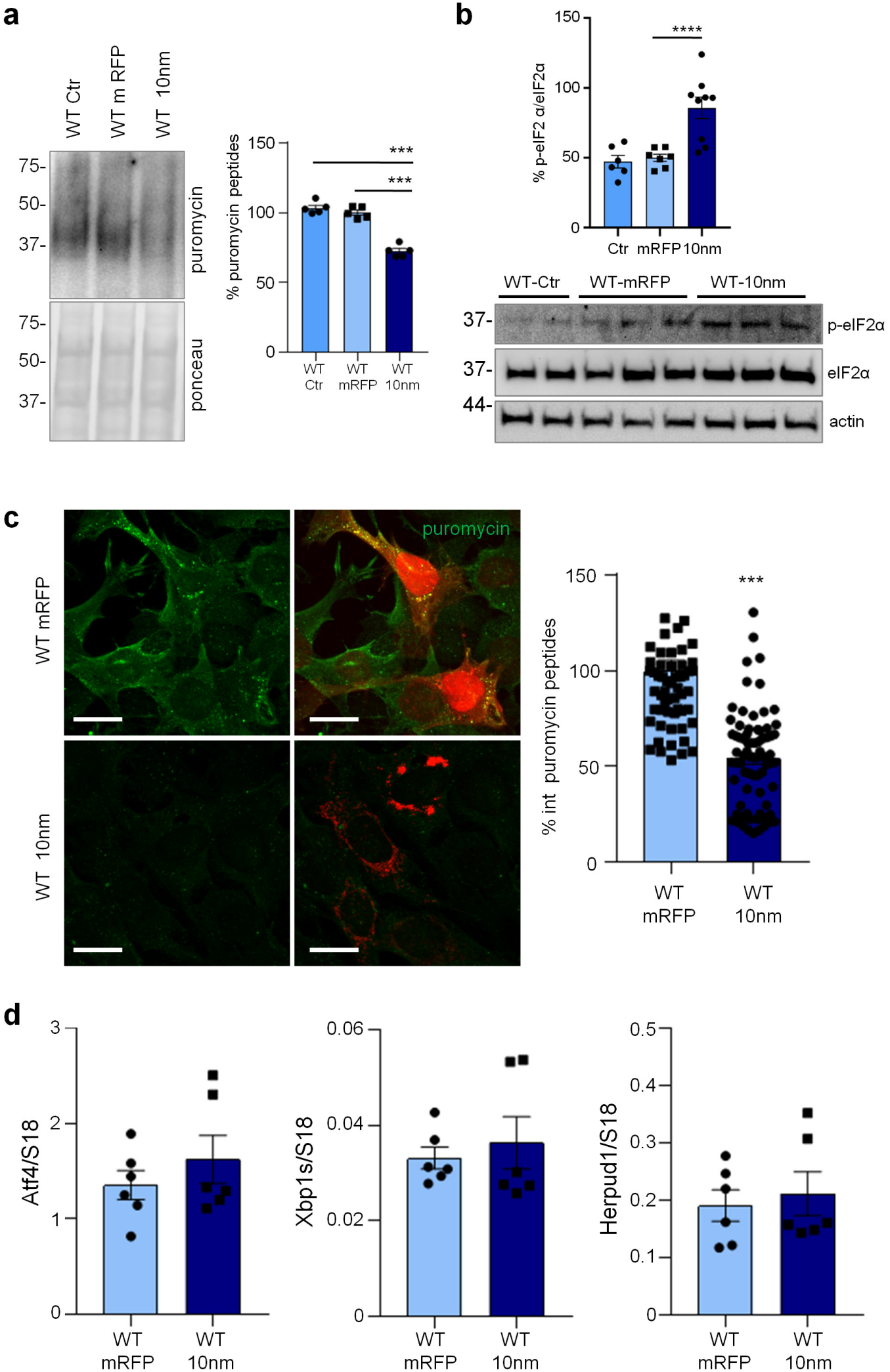
a
WT Ctr
WT m RFP
WT 10nm
75-
50-
37-
puromycin
ponceau
% puromycin peptides
150
100
50
0
***
***
WT Ctr
WT mRFP
WT 10nm
b
% p-eIF2 α/eIF2α
****
Ctr
mRFP
10nm
WT-Ctr
WT-mRFP
WT-10nm
37-
44-
p-eIF2α
eIF2α
actin
c
WT mRFP
WT 10nm
puromycin
% int puromycin peptides
***
d
Atf4/S18
Xbp1s/S18
Herpud1/S18
3
2
1
0
0.06
0.04
0.02
0.5
0.4
0.3
0.2
0.1

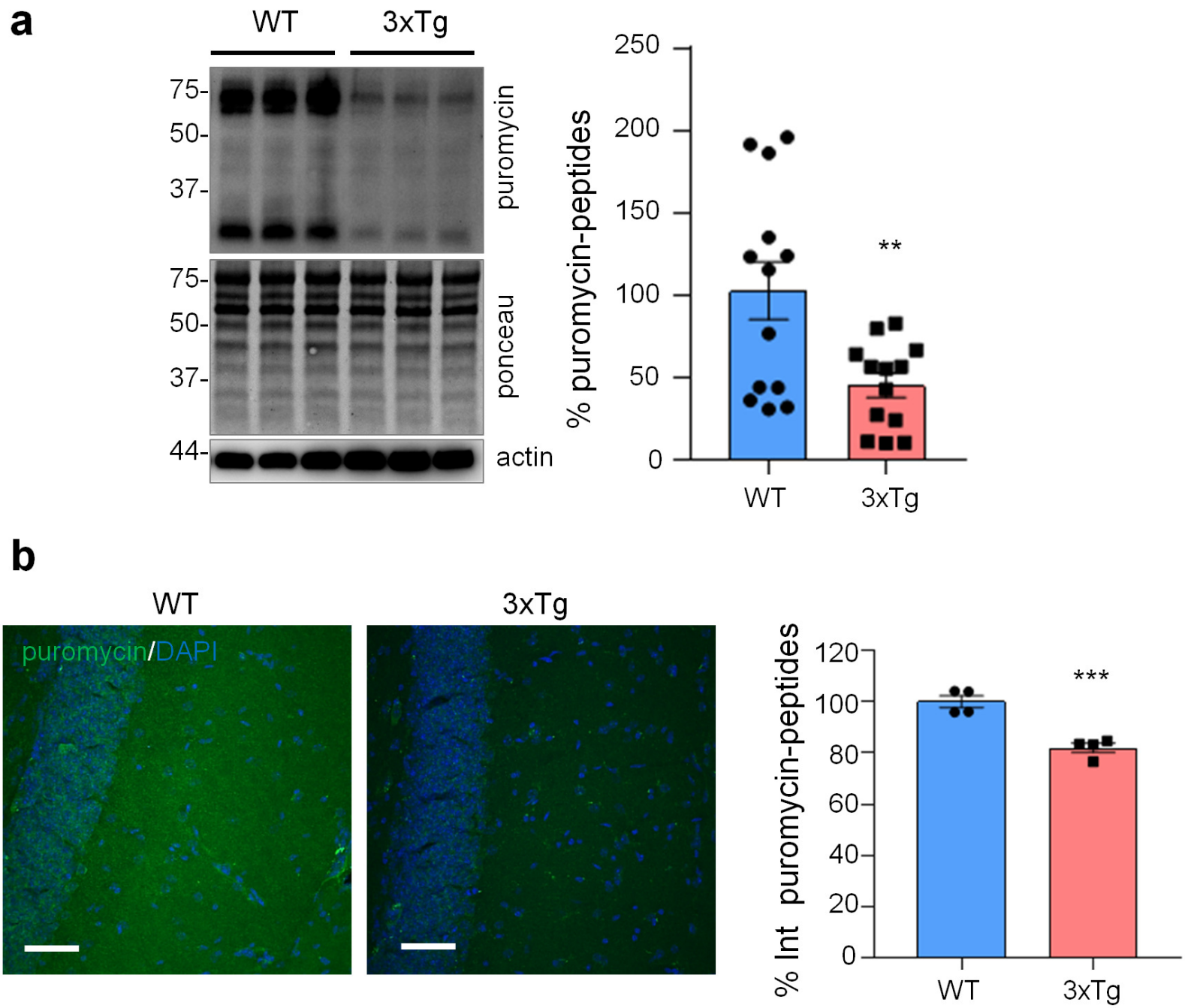
a
WT
3xTg
75-
50-
37-
puromycin
75-
50-
37-
ponceau
44-
actin
% puromycin-peptides
250
200
150
100
50
0
**
WT
3xTg
b
WT
3xTg
puromycin/DAPI
% Int puromycin-peptides
120
100
80
60
40
20
0
***
WT
3xTg

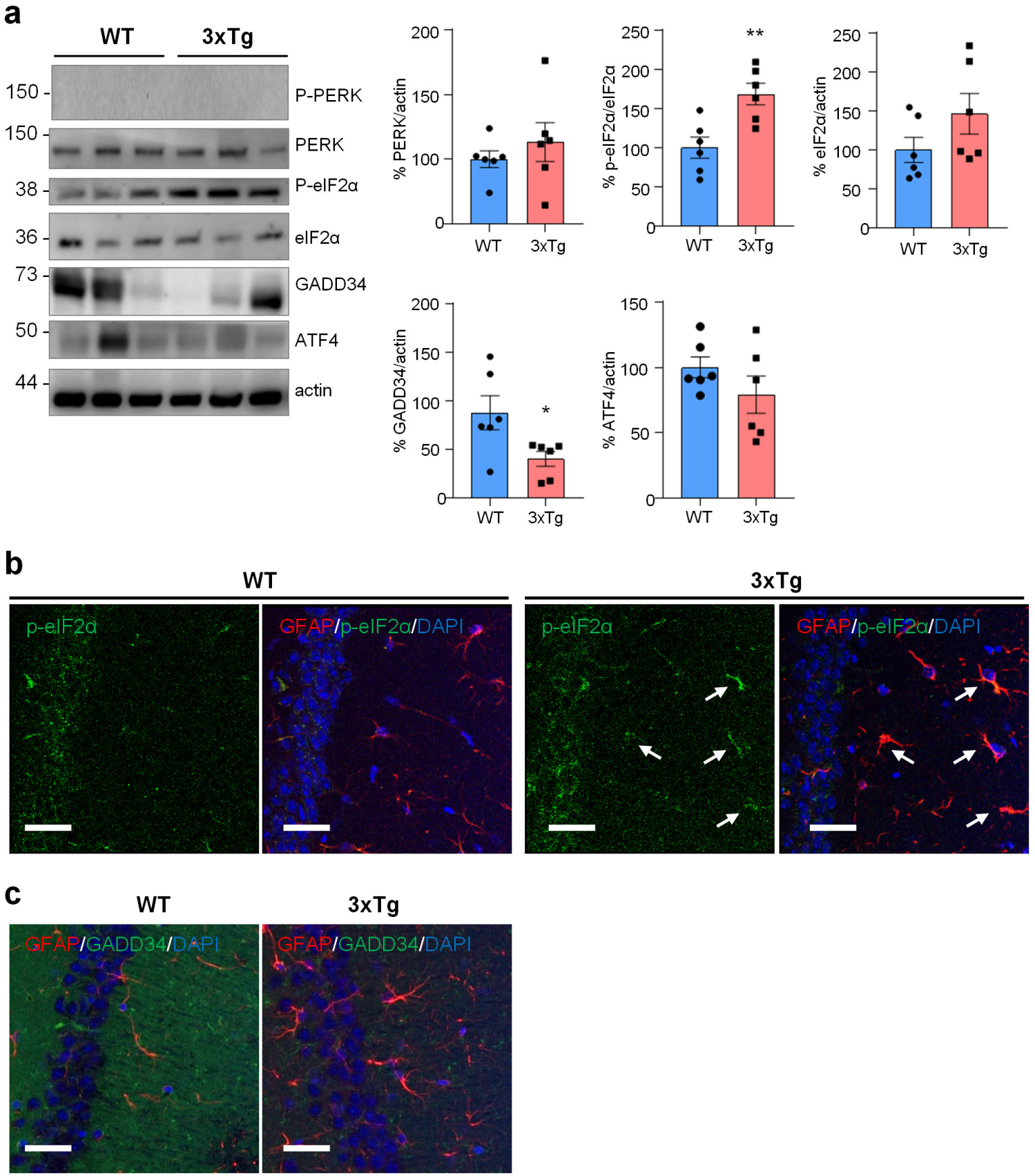
a
WT
3xTg
150
P-PERK
150
PERK
38
P-eIF2α
36
eIF2α
73
GADD34
50
ATF4
44
actin
% PERK/actin
% p-eIF2α/eIF2α
% eIF2α/actin
% GADD34/actin
% ATF4/actin
**
*
b
WT
3xTg
p-eIF2α
GFAP/p-eIF2α/DAPI
c
GFAP/GADD34/DAPI
d
Atf4/S18
Xbp1/S18
Herud1/S18

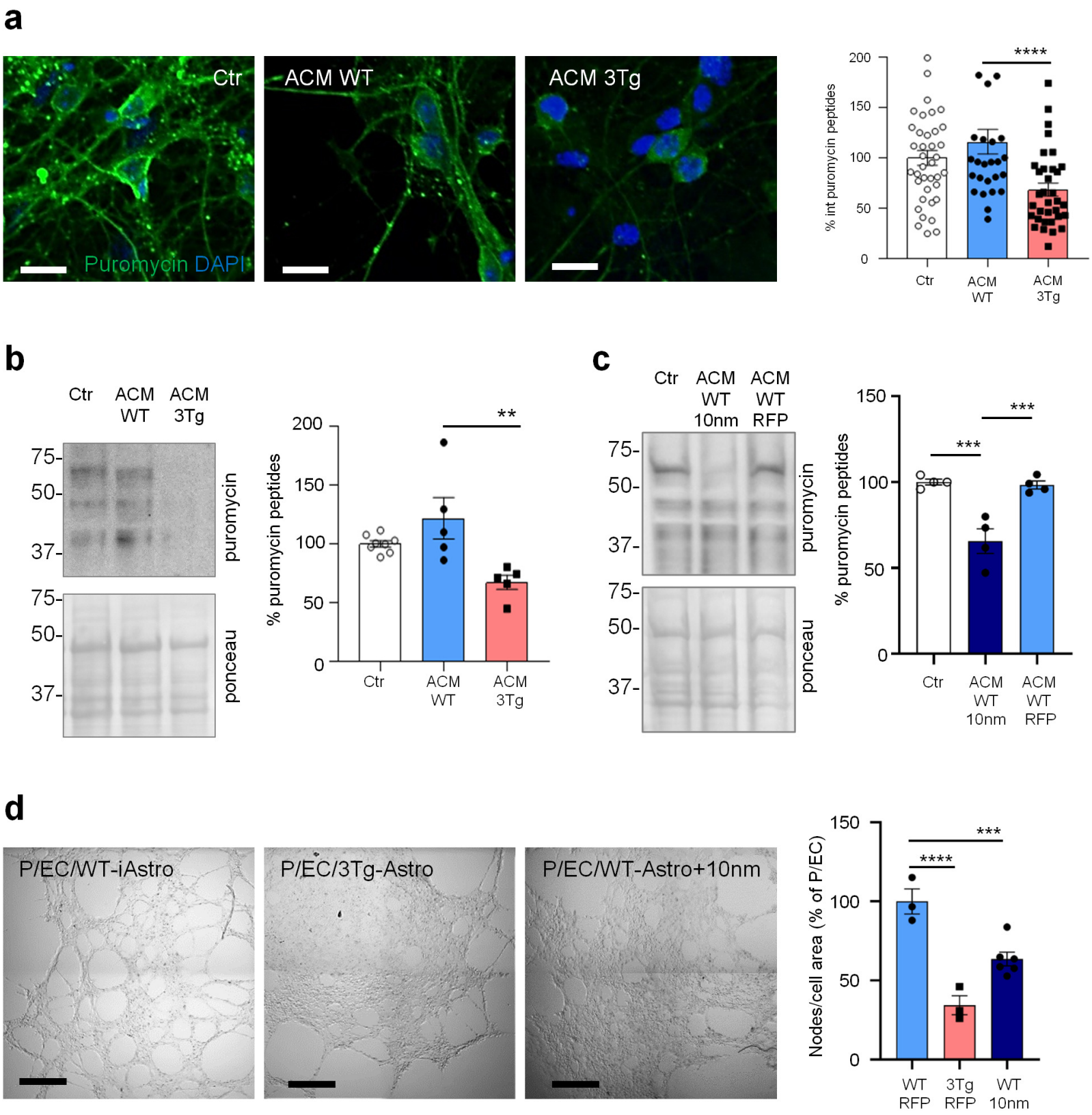
a
Ctr
ACM WT
ACM 3Tg
Puromycin DAPI
% int puromycin peptides
200
150
100
50
0
****
Ctr
ACM WT
ACM 3Tg
b
Ctr
ACM WT
ACM 3Tg
75-
50-
37-
puromycin
ponceau
% puromycin peptides
**
c
Ctr
ACM WT 10nm
ACM WT RFP
***
d
P/EC/WT-iAstro
P/EC/3Tg-Astro
P/EC/WT-Astro+10nm
Nodes/cell area (% of P/EC)
WT RFP
3Tg RFP
WT 10nm

Differentially expressed proteins
3Tg vs WT

Protein	Uniprot_ID	FC	p.v.
FABP3	FABPH_MOUSE	+4.7	0.04
SPARC	SPRC_MOUSE	-1.6	0.03
HSP90	HS90B_MOUSE	-2.1	0.04
HSP73	HSP7C_MOUSE	-2.3	0.04
Tub-α1b	TBA1B_MOUSE	-3.9	0.02

Identified proteins

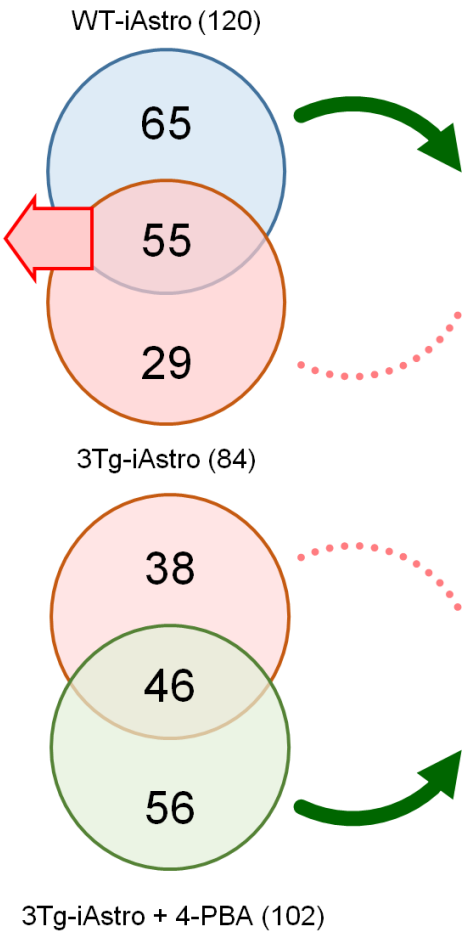

GO terms overrepresented in WT but not in 3Tg

Term	Count	Fold Enr	Adj.p.v.
GOTERM: Cellular Component			
GO:0031012~extracellular matrix	16	16.7	1.18E-12
GO:0005925~focal adhesion	15	11.8	8.76E-10
GO:0005913~cell-cell adherens junction	12	11.7	1.43E-07
GOTERM: Molecular Function			
GO:0098641~cadherin binding involved in cell-cell adhesion	12	12.1	6.92E-07
GOTERM: KEGG Pathway			
mmu04510:Focal adhesion	8	6.1	0.012

GO terms overrepresented in 3Tg + 4-PBA but not in 3Tg

Term	Count	Fold Enr	Adj.p.v.
GOTERM: Biological Process			
GO:0042060~wound healing	6	20.0	0.0054
GO:0030199~collagen fibril organization	5	33.7	0.0054
GOTERM: Cellular Component			
GO:0005615~extracellular space	24	4.6	2.40E-08
GO:0031012~extracellular matrix	8	10.6	2.94E-04
GO:0005581~collagen trimer	5	23.3	0.0017
GOTERM: Molecular Function			
GO:0030020~extracellular matrix structural constituent	4	38.0	0.0056
GO:0005201~extracellular matrix structural constituent	5	15.0	0.0099
GO:0005518~collagen binding	4	17.8	0.033

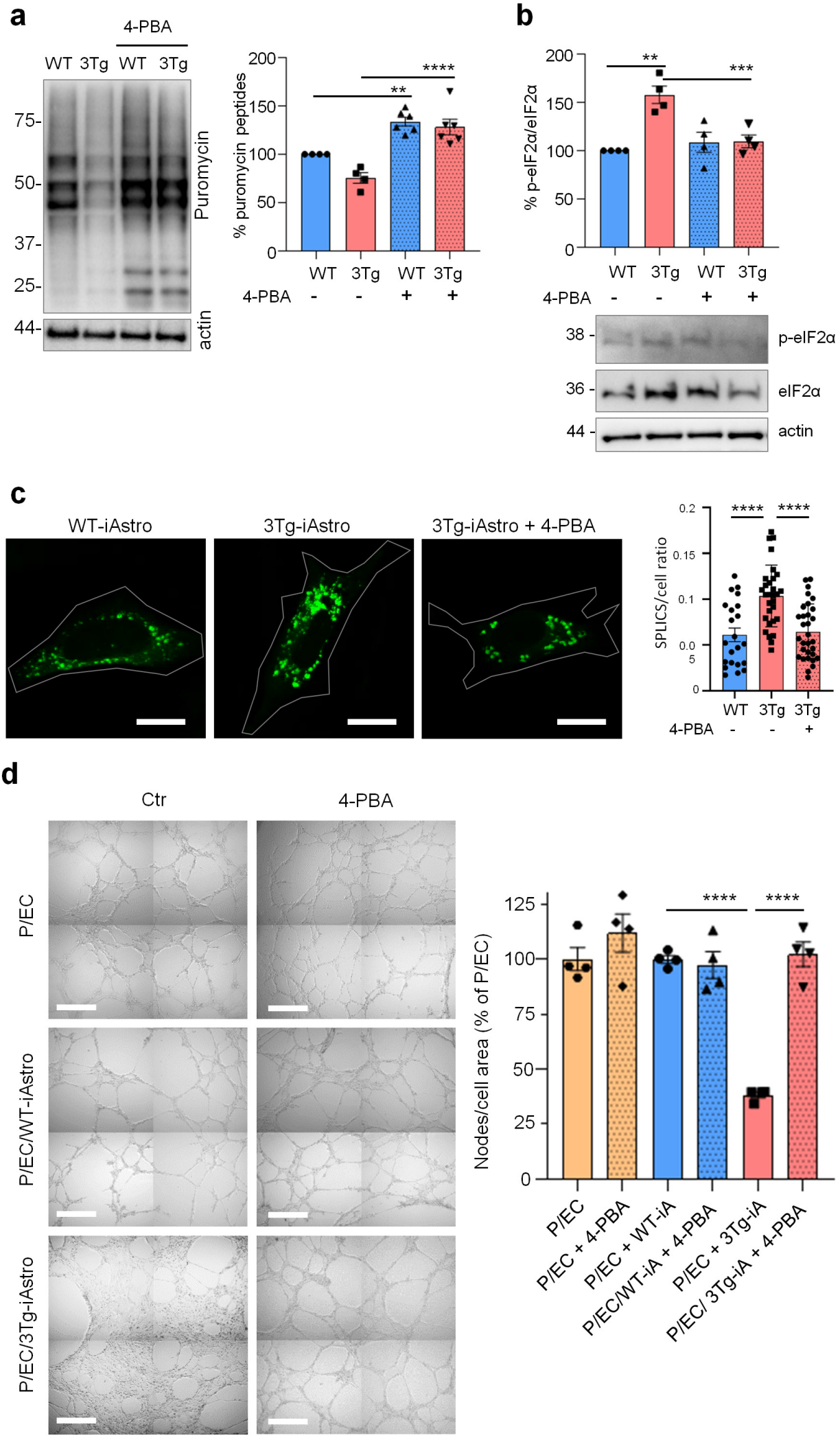
a
4-PBA
WT 3Tg WT 3Tg
75-
50-
37-
25-
44-
Puromycin
actin
% puromycin peptides
200
150
100
50
0
**
****
WT 3Tg WT 3Tg
4-PBA - - + +
b
% p-eIF2α/eIF2α
200
150
100
50
0
**
***
WT 3Tg WT 3Tg
4-PBA - - + +
38 -
p-eIF2α
36 -
eIF2α
44 -
actin
c
WT-iAstro
3Tg-iAstro
3Tg-iAstro + 4-PBA
SPLICS/cell ratio
0.2
0.15
0.1
0.05
0
****
****
WT 3Tg 3Tg
4-PBA - - +
d
Ctr
4-PBA
P/EC
P/EC/WT-iAstro
P/EC/3Tg-iAstro
Nodes/cell area (% of P/EC)
125
100
75
50
25
0
****
****
P/EC
P/EC + 4-PBA
P/EC + WT-iA
P/EC/WT-iA + 4-PBA
P/EC + 3Tg-iA
P/EC/ 3Tg-iA + 4-PBA

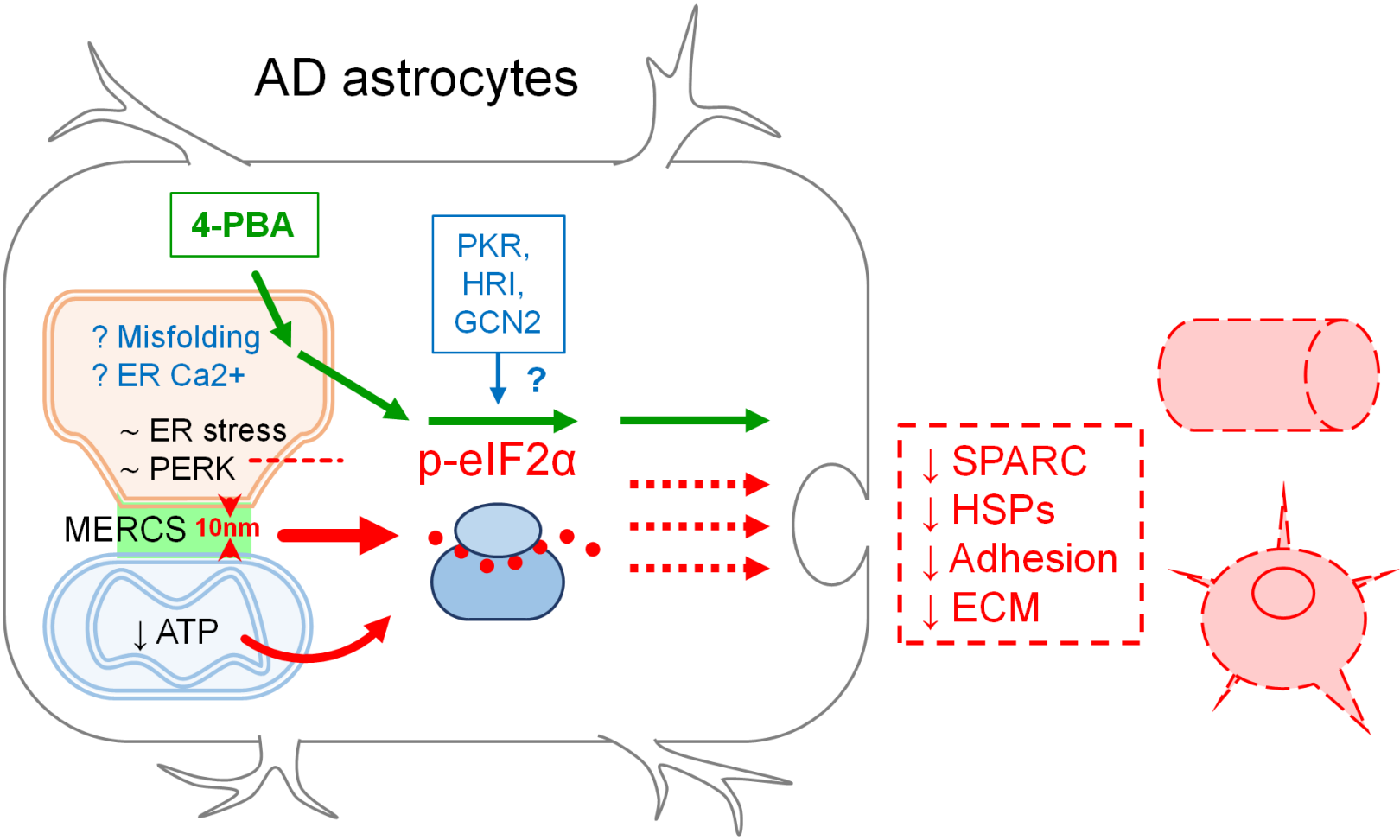
AD astrocytes
4-PBA
PKR,
HRI,
GCN2
?
? Misfolding
? ER Ca2+
~ ER stress
~ PERK
MERCS
10nm
↓ ATP
p-eIF2α
↓ SPARC
↓ HSPs
↓ Adhesion
↓ ECM